small method
www.small-methods.com



# Lattice Vibration and Raman Scattering in Anisotropic Black Phosphorus Crystals

*Nannan Mao, Shuqing Zhang, Juanxia Wu, Jin Zhang,* and Lianming Tong**

**Here, an overview of recent advances on the Raman spectroscopic studies of 2D black phosphorus (BP) crystals is provided, covering the fundamentals of Raman scattering such as the crystal symmetry and the assignment of the phonon modes, the Raman selection rule that can be used to determine the crystalline orientation, the interlayer coupling that gives rise to the interlayer shear and breathing modes, and the effects of perturbation such as temperature, strain, and pressure. Due to the low in-plane symmetry of BP, particular attention is given to the anisotropic electron–photon and electron–phonon interactions in BP, which have strikingly distinct characteristics compared with other isotropic 2D materials. The abnormal polarized Raman scattering of anisotropic BP crystals and its dependence on the excitation energy, thickness, and phonon modes are discussed from the viewpoints of the complex Raman tensors and the optical birefringence effect. Furthermore, the calibration of the Raman selection rule in anisotropic BP crystals is discussed, and the versatility of Raman spectroscopy in characterizing the structure of BP, such as the layer number, the type of edges, and the crystalline orientation are considered.**

## 1. Introduction

Black phosphorus (BP), a remarkable elemental semiconductor with lamellar structure, has attracted significant attentions in the past three years.[1] Unlike other allotropes of phosphorus, such as red phosphorus and white phosphorus, BP possesses a puckered structure, where the $sp^3$ hybridized P atoms form zigzag chains by connecting to the nearest P atoms.[2] The relaxed restriction of the bond angle in such a puckered structure makes BP the most thermodynamically stable allotrope of phosphorus. Recently, BP has been reintroduced into the 2D materials community as a p-type semiconductor with exceptionally high carrier mobility and considerable on–off ratios.[1b] The predicted carrier mobility is as high as 10 000 to 26 000 $cm^2\ V^{-1}\ s^{-1}$, and current experimental measurements have reached 4000–6000 $cm^2\ V^{-1}\ s^{-1}$.[1d,3] In addition, BP is among the few less-known 2D layered crystals with direct bandgaps in both monolayer and multilayer forms.[1d,f,m,4] Owing to its strong interlayer interaction, BP exhibits extraordinary layer-dependent electronic structures with bandgaps varying from infrared (0.35 eV) to visible region (1.73 eV).[1h,m] Unlike most other well-studied layered crystals with isotropic in-plane lattice, BP has an anisotropic puckered structure that is stiff along one of the in-plane directions (zigzag) but flexible along the other (armchair).[1d] As a result, BP has shown significant anisotropy in electrical, optical, mechanical, and thermal properties.[1d,f,g,4b,5] In addition, BP has shown anisotropic electron and phonon dispersion, which give rises to the anisotropic electron–photon and electron–phonon interactions.[1d,f,5f,6] Considering all of these properties, BP is a promising candidate for field-effect transistors, broad-band polarization-dependent photodetectors, and optical modulators.[1a,b,i,j,7]

Raman spectroscopy is a fast and nondestructive characterization tool that provides structural and chemical information of materials. Even though they have a small effective scattering cross section, most nanomaterials show considerable Raman signal due to resonance effects and interference enhancement.[8] In recent years, Raman spectroscopy has demonstrated its powerful capability in characterizing 2D layered materials. Taking graphene as an example, Raman spectroscopy has revealed rich information on the chemical and electronic structure of graphene: the layer number and stacking order, the type of edges, the doping type, disorder and defects, and the interlayer interactions.[9] In addition, Raman spectroscopy has also been used to probe the electron–photon and electron–phonon interactions in the Brillouin zone center, and to investigate the basic physicochemical properties such as the thermal conductivity.[9e,10]

Here, we highlight the recent advances in the Raman scattering studies of 2D BP crystals. First, we introduce the basic concept of the atomic structure and discuss the crystal symmetry, lattice vibration, phonon dispersion, and layer-number dependence of the Raman spectra of BP. Then, we emphasize the anisotropic electron–photon and electron–phonon interactions in the orthorhombic BP crystal and review recent studies of the anomalous polarized Raman scattering in BP and its dependence on the excitation energy, thickness, and

Dr. N. Mao, Dr. S. Zhang, Dr. J. Wu, Prof. L. Tong, Prof. J. Zhang
Center for Nanochemistry
Beijing Science and Engineering Center for Nanocarbons
State Key Laboratory for Structural Chemistry of Unstable and Stable Species
College of Chemistry and Molecular Engineering
Peking University
Beijing 100871, P. R. China
E-mail: jinzhang@pku.edu.cn; tonglm@pku.edu.cn
The ORCID identification number(s) for the author(s) of this article can be found under https://doi.org/10.1002/smtd.201700409.

**DOI: 10.1002/smtd.201700409**

phonon modes. Finally, we summarize the interlayer shear and breathing modes, edge phonons, and phonon behavior under external perturbation such as temperature, strain, and pressure. We emphasize the Raman scattering characteristic of BP associated with its in-plane low symmetry, give examples of the versatility of Raman spectroscopy in characterizing the layer number, edges, crystalline orientation, and interlayer interaction of BP, and hope to provide a complete understanding of the Raman scattering of 2D materials with in-plane low symmetry in general.

## 2. Structure Symmetry, Lattice Vibrations, and Phonon Dispersion

To understand the Raman scattering and Raman selection rule in 2D anisotropic BP crystals, it is important to know the symmetry of its atomic structure, lattice vibrations, and phonon dispersion.

Elemental phosphorus exists in several forms with strikingly different atomic structures. Distinct from the tetrahedral P4-based structure of other phosphorus allotropes, BP presents a layered structure with each $sp^3$ hybridized P atom covalently bonded to three nearest neighbors in the layer (P1–P2 or P1–P3 bond at 2.22 Å and P1–P4 at 2.28 Å, see **Figure 1**a,b). Each puckered layer is stacked on top of each other through van der Waals forces along the *z*-direction, forming a lamellar structure with the interlayer distance being 3.27 Å. The bond angles ∠P3P1P2 (96.5°) and ∠P3P1P4 (101.9°) are much larger than the bond angles in white and red phosphorus, suggesting less strain and better stability.[2a] The experimental lattice parameters of orthorhombic BP structure are $x = 3.31$, $y = 10.47$, and $z = 4.37$ Å.[2a]

In general, group theory is used to predict the normal modes in crystals, and the lattice vibrations are classified by the irreducible representations of the symmetry group of the corresponding crystals. The research of the lattice dynamical properties of BP can be traced back to 1980s.[12] The research methods at that time included calculations using a valence force model,[12a,d] inelastic neutron-scattering measurements,[12b] and infrared and Raman vibrational optical spectroscopy.[12c,13] Bulk BP crystallizes in a base-centered orthorhombic structure with the space group of *Cmca* (No. 64, $D_{2h}^{18}$) in the Hermann–Mauguin (Schoenflies) notation.[14] The corresponding first Brillouin zone and calculated phonon dispersion[12d] are shown in **Figure 2**a,b. Research of *N*-layer BP has been emerging during the past three years.[1b,p] For *N*-layer BP, its symmetry is dependent on whether the number of layers is even or odd. The unit cell of *N*-layer BP is a simple rectangle, so the Brillouin zone is also a rectangle, as shown in the inset of Figure 2c, and the space groups for odd and even layers are subgroups of the bulk space group. The space group is *Pbmn* ($D_{2h}^{7}$) for *N* odd layers, and *Pbma* ($D_{2h}^{11}$) for *N* even layers. There are 4*N* atoms for an *N*-layered sample, thus 12*N* vibrational modes, including 3 acoustic and 12*N* − 3 optical modes.[15] Following the conventional coordinates system for bulk BP, the *x*- and *z*-axes correspond to armchair and zigzag directions, and the irreducible representations of Brillouin zone center (Γ) for *N*-layer BP is given by: $N(2A_g + B_{1g} + B_{2g} + 2B_{3g} + A_u + 2B_{1u} + 2B_{2u} + B_{3u})$.[5f,16] The swapped use of subscripts 2 and 3 in some reports in the literature comes from the different definitions of the crystal coordinate system.[15b,17] For single-layer BP, the primitive cell consists of four atoms, suggesting 12 vibrational modes in total (three acoustic and nine optical phonons). The calculated phonon dispersion of single-layer BP and the optical phonon vibration patterns are shown in Figure 2c,d.[5c,18] The phonon dispersion of monolayer

**Nannan Mao** received her B.S. degree in chemistry from Lanzhou University in 2011 and her Ph.D. degree in physical chemistry from Peking University in 2016. She is now a postdoctoral associate in Prof. Mildred S. Dresselhaus's group and Prof. Jing Kong's group at Massachusetts Institute of Technology. Her current research is focused on the Raman spectroscopy of 2D anisotropic crystals.

**Jin Zhang** was appointed as Changjiang Professor at Peking University, China, in 2013. He received his Ph.D. degree in chemistry from Lanzhou University, China, in 1997. After a postdoctoral fellowship at the University of Leeds, UK, he returned to Peking University, where he was appointed associate professor in 2000 and promoted to a full professor in 2006. He is a fellow of the Royal Society of Chemistry. His research focuses on the controlled synthesis and spectroscopic characterization of carbon nanomaterials.

**Lianming Tong** received his B.S. and Ph.D. degrees in chemistry from Peking University, China, in 2002 and 2007, respectively. He was an associate professor at the Institute of Physics, Chinese Academy of Sciences from 2011 to 2015. He is now an associate professor in the College of Chemistry and Molecular Engineering, Peking University. His research interests include Raman spectroscopy of low-dimensional materials and surface-enhanced Raman spectroscopy (SERS).

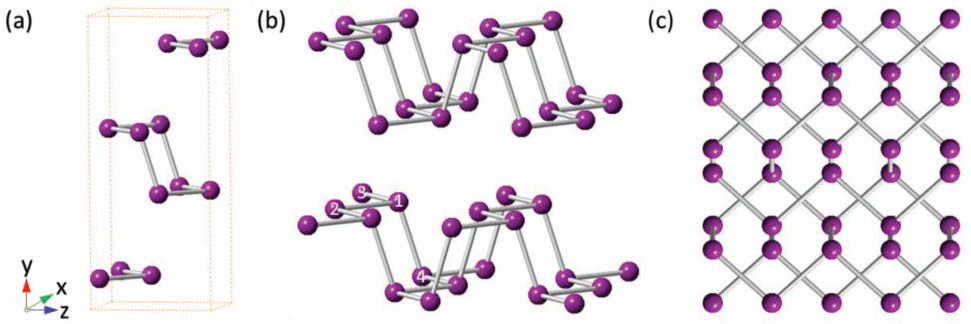


**Figure 1.** a) Unit cell of the bulk black phosphorus. b,c) Oblique view (b) and top view (c) of the atomic structure of black phosphorus. c) Reproduced with permission.[11] Copyright 2016, Wiley-VCH.

BP shows nine optical phonon branches and three acoustic branches, including the out-of-plane acoustic modes, the in-plane transverse acoustic modes, and the longitudinal acoustic modes.[5c] The space group classification of the bulk phase is different from that of few-layer, because there is an additional type of symmetry in the perpendicular direction for bulk BP. Nevertheless, they belong to the same $D_{2h}$ point group.[15b,16a] Bulk BP has four atoms in the primitive cell, and its irreducible representations are the same as single-layer BP.[15,16] According to the irreducible representations of the $D_{2h}$ point group, the normal modes of BP crystals at the T-point can be expressed as follows: $\Gamma = (2A_g + B_{1g} + B_{2g} + 2B_{3g} + A_{1u} + 2B_{1u} + 2B_{2u} + B_{3u})$. Among the above modes, one $B_{1u}$, one $B_{2u}$, and one $B_{3u}$ modes are acoustic modes, while the others are optical modes. For the optical modes, all the even parity modes, denoted as $A_g^1$, $A_g^2$, $B_{1g}$, $B_{2g}$, $B_{3g}^1$, and $B_{3g}^2$, are first-order Raman active modes and all are nondegenerate;[12c,16b] the other $B_{1u}$ and $B_{2u}$ modes are infrared-active modes, and the $A_{1u}$ mode is inactive.[19] As shown in Figure 2d, the $B_{1g}$, $B_{2g}$, and $B_{3g}^1$ modes are in-plane vibrational modes; the $B_{1g}$ and $B_{2g}$ modes correspond to vibrations along the zigzag direction, whereas $B_{3g}^1$ is related to the vibrations along the armchair direction. In contrast, $B_{3g}^2$ is an out-of-plane vibrational mode.[18] It is also indicated in Figure 2d that the $A_g^1$ and $A_g^2$ modes involve both the in-plane and out-of-plane vibrations. However, the $A_g^1$ mode has a larger component along the out-of-plane direction, whereas the $A_g^2$ mode is dominated by in-plane vibration along the armchair direction, and will evolve into a pure in-plane vibration with increasing layer number.[20]

Besides the Raman activity, an appropriate measurement configuration is also critical for the observation of Raman modes.[12c,16b] The normal configuration in experiment is back-scattering geometry. As shown in **Figure 3**a, only the $A_g$ and $B_{2g}$ modes are visible in this configuration. Therefore, the typical Raman spectra of BP crystals only have three characteristic Raman peaks: $A_g^1$ (363 $cm^{-1}$), $B_{2g}$ (440 $cm^{-1}$), and $A_g^2$ (467 $cm^{-1}$).[1g,16c] Of course, here the interlayer modes in few-layer BP, which appear in the low-frequency range are not taken into account.[5c,15a,17b] In a conventional Raman measurement, the propagation direction of the incident laser is perpendicular to the cleavage plane (*xz*) of the BP layers, no matter whether the samples are prepared through mechanical or solvent exfoliation methods. According to the Raman selection rule of BP, the Raman tensors of $B_{3g}^1$ (230 $cm^{-1}$), $B_{3g}^2$ (436 $cm^{-1}$), and

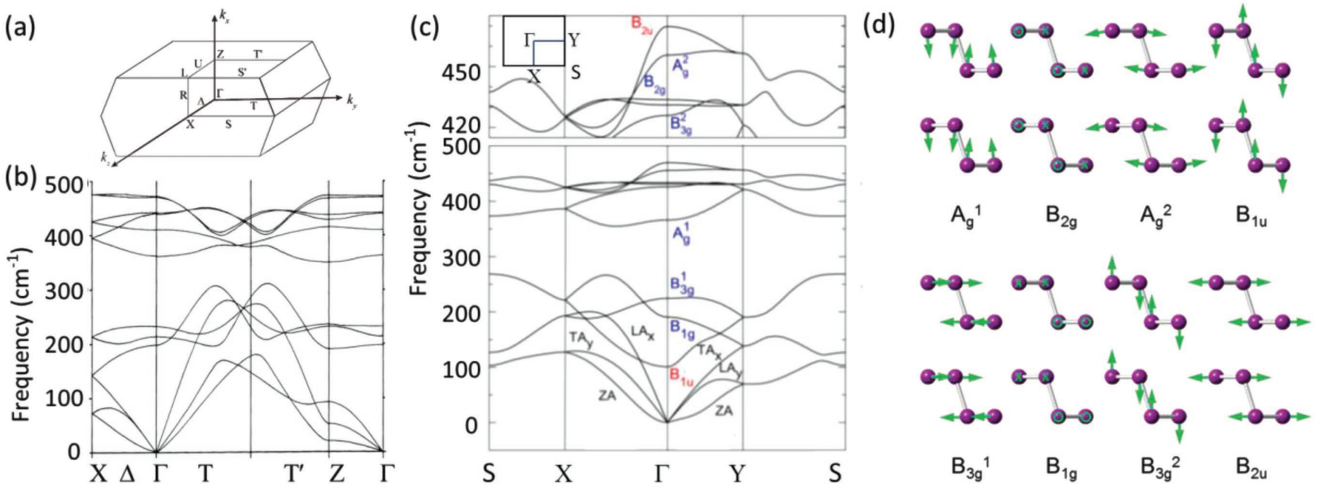


**Figure 2.** a) The first Brillouin zone of bulk BP. b) The calculated phonon-dispersion curves of bulk BP based on the valence force field model. a,b) Reproduced with permission.[12d] Copyright 1986, Physical Society of Japan. c) The phonon-dispersion curves of single-layer BP using first-principles calculation. The inset represents the first Brillouin zone of 2D layered BP. Reproduced with permission.[5c] Copyright 2015, Wiley-VCH. d) The vibration patterns of the optical modes of single-layer BP. Reproduced with permission.[11] Copyright 2016, Wiley-VCH.

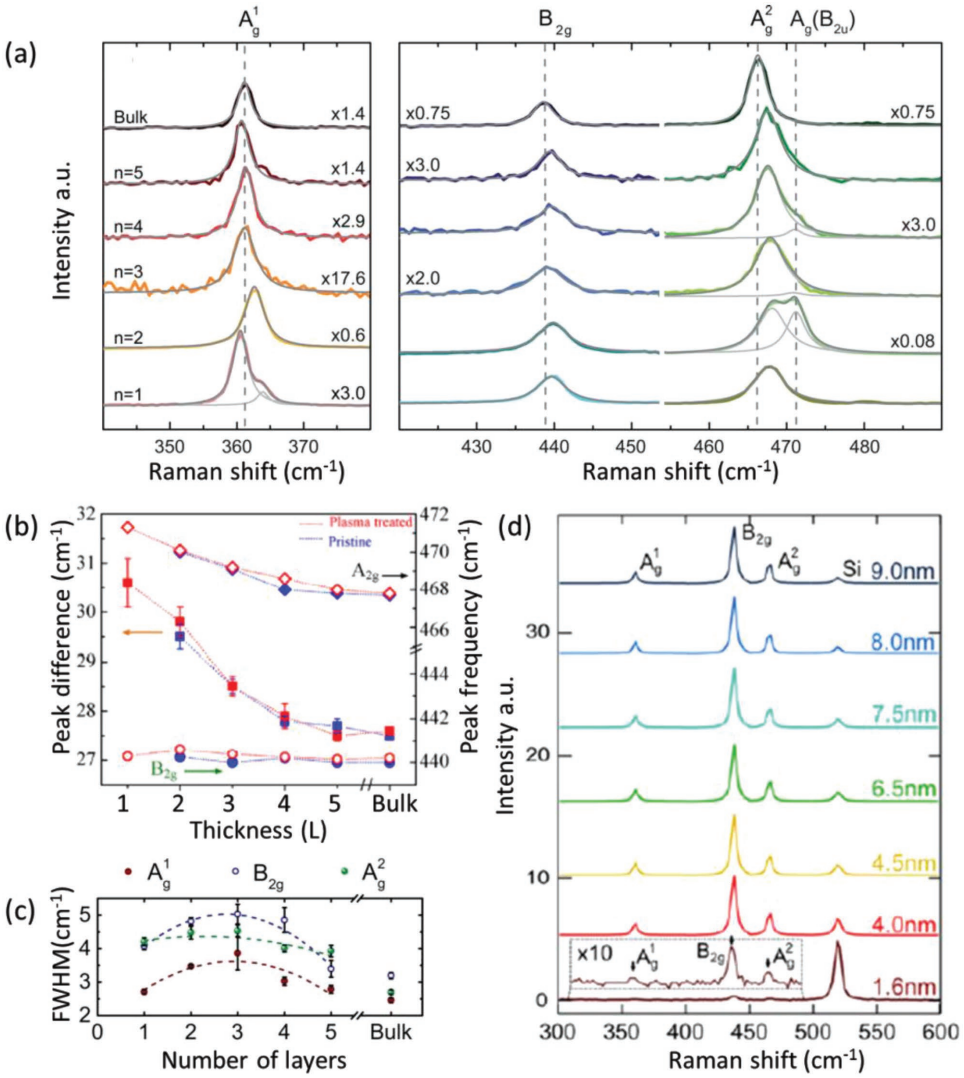


**Figure 3.** a) The typical Raman spectra of few layer (1–5L) and bulk BP. Reproduced with permission.[21] Copyright 2016, American Chemical Society. b) Raman frequencies and the frequency difference of $A_g^2$ and $B_{2g}$ modes for pristine exfoliated BP sample and plasma-treated ones as a function of thickness. Reproduced with permission.[1c] Copyright 2014, Springer. c) Full-width at half-maximum (FWHM) of $A_g^1$, $B_{2g}$, and $A_g^2$ modes with increasing thickness of BP crystals. Reproduced with permission.[21] Copyright 2016, American Chemical Society. d) Raman spectra for the different regions of a BP flake with thicknesses ranging from 1.6 to 9.0 nm. The inset shows the zoomed-in Raman spectra for 1.6 nm thick BP. Reproduced with permission.[22] Copyright 2014, IOP Publishing.

$B_{1g}$ (194 $cm^{-1}$) modes do not contain the effective $\mathbf{R}_{xz}/\mathbf{R}_{zx}$ and $\mathbf{R}_{yz}/\mathbf{R}_{zy}$ component. Therefore, they are not allowed in the back-scattering configuration. However, if the BP crystal is excited by an oblique incident laser with a polarization component parallel to the BP plane, these bands will appear in the spectrum. This is related to the Raman selection rule of BP, which will be discussed in the subsequent section.

## 3. Layer-Number-Dependent Raman Scattering

Due to the van der Waals interaction between layers of BP, adding an additional puckered layer on the existing BP layers will induce a slight change of the lattice parameters and the corresponding electronic structure. Consequently, the Raman scattering process in BP, which is related to photon–electron and phonon–electron interactions, is expected to exhibit a strong layer-number dependence.

Lu et al. first reported the Raman spectra of 1–5 L BP and bulk BP on 300 nm $SiO_2$/Si substrates, where monolayer BP was obtained by plasma-assisted fabrication, and few-layer BP samples were mechanically exfoliated.[1c] The Raman intensities of the three bands ($A_g^1$, $B_{2g}$, and $A_g^2$) increase monotonically with the layer number of BP. The intensity ratio between the $A_g^1$ mode and the first-order Si peak also undergoes a monotonic increase as the layer number increases from 1L to 5L.[1c] In addition, there is a slight redshift (up to 2 $cm^{-1}$) of the $A_g^2$ mode from monolayer to five layers, while the $A_g^1$ and $B_{2g}$ modes remain almost constant (Figure 3b). The stiffening of the $A_g^2$ mode as the thickness decreases is

attributed to the van der Waals stacking-induced anisotropic structural relaxation.[1c,23] The $A_g^1$ mode is dominated by the atomic vibration along the out-of-plane direction, and the $A_g^2$ mode is dominated by in-plane vibration along the armchair direction.[12c,13] Previous reports have predicted that the lattice parameter along the armchair direction decreases significantly from monolayer to bulk, while other lattice parameters along the other crystalline directions remain almost unchanged.[1d,5c,20,24] Therefore, the $A_g^2$ mode is more sensitive to the layer number than the $B_{2g}$ and $A_g^1$ modes. As shown in Figure 3a,c, Phaneuf L'Heureux et al. and Favron et al. discovered that few-layer BP shows a nonmonotonic evolution in width and position when the thickness decreases to monolayer.[21,25] The broadening of these three Raman modes increases from 5L to 3L, and reaches maximum at 3L; then it decreases gradually from 3L to monolayer BP. It is reported that Raman peaks of amorphous BP also become broader in thinner samples.[7i] Apparently, two additional Raman modes appear in the Raman spectra of BP. The mode located at the high-frequency shoulder of the $A_g^1$ mode is related to a second-order Raman process. The other mode, separated from the $A_g^2$ mode, is assigned to the Davydov-induced conversion from an IR-active mode ($B_{2u}$) to a Raman-active mode ($A_g$).[21] For even thicker BP crystals (from 1.6 to 9.0 nm), as shown in Figure 3d, the Raman peaks of these three modes do not exhibit a noticeable shift when the thickness increases. Nonetheless, the intensity ratio between the $A_g^1$ band and the silicon Raman peak (520 $cm^{-1}$) is proportional to the thickness of the BP sample.[22]

The evolution of the Raman peaks with respect to the thickness of few-layer 2D materials has been widely exploited to identify the layer number. However, this method does not apply to BP because the high-frequency Raman modes just shift very slightly with its thickness. In addition, since the laser commonly used for Raman measurements is linearly polarized, and the Raman intensities of both the BP and the silicon peaks depend on the sample rotation angle and laser polarization, it is rather complicated to identify the layer number according to the intensity ratio between the $A_g^1$ mode and first-order Si peak, unless the BP flakes to be measured remain in the same crystalline orientation.[16c,22,23]

## 4. Raman Selection Rule for Phonons in Anisotropic BP Crystal

### 4.1. Normal Raman Selection Rule

The emergence of a phonon mode is determined by the symmetry of the phonon, the experimental geometry of the incident and detection directions relative to the principal axes of the crystal. According to the classical Placzek approximation,[26] the Raman scattering efficiency of a phonon is proportional to $|\mathbf{e}_i \cdot \mathbf{R} \cdot \mathbf{e}_s|^2$, where $\mathbf{e_i}$ and $\mathbf{e_s}$ are the polarization vectors of the incident and scattered light, $\mathbf{R}$ is the second-rank polarizability tensor for different phonons in space-fixed coordinates, usually called Raman tensor.[26a] The Raman tensors of the $A_g$, $B_{1g}$, $B_{2g}$, and $B_{3g}$ phonon modes in BP crystal are expressed as[13]

$$\mathbf{R}(A_g) = \begin{pmatrix} a & 0 & 0 \\ 0 & b & 0 \\ 0 & 0 & c \end{pmatrix} \quad \mathbf{R}(B_{1g}) = \begin{pmatrix} 0 & d & 0 \\ d & 0 & 0 \\ 0 & 0 & 0 \end{pmatrix} \tag{1}$$

$$\mathbf{R}(B_{2g}) = \begin{pmatrix} 0 & 0 & e \\ 0 & 0 & 0 \\ e & 0 & 0 \end{pmatrix} \quad \mathbf{R}(B_{3g}) = \begin{pmatrix} 0 & 0 & 0 \\ 0 & 0 & f \\ 0 & f & 0 \end{pmatrix} \tag{2}$$

Since the Raman tensor of a crystal is determined by the phonon symmetry and the crystal symmetry, the Raman efficiency of a phonon is dependent on not only the polarization directions of the incident and scattered light but also the crystalline orientation. Two different approaches are commonly used to measure the polarized Raman scattering of BP:[27] one is to rotate the polarization of the incident and scattered light while keeping the sample fixed (method I);[1g,l,24b,28] the other is to rotate the sample with fixed polarizations (method II).[1l,5f,11,15a,16c,29] Generally speaking, the polarization configurations for polarized Raman scattering are usually denoted as the term $A(BC)\bar{A}$, where $A$ and $\bar{A}$ refer to the propagation directions of the incident laser and scattered Raman signals, $B$ and $C$ denote the polarization directions of the incoming laser and the analyzer. Under most circumstances, the polarized Raman scattering measurements of BP crystals are carried out in the back scattering geometry, where $e_i$ and $e_s$ are within the cleavage plane. For the polarized Raman spectra measured by rotating the incident polarization without an analyzer,[1g,24b,28a] $I(A_g) = |e_i\mathbf{R}|^2 = a^2\sin2\alpha + c^2\cos2\alpha$, $I(B_{2g}) = e^2$, where $\alpha$ is the rotation angle of the incident polarization ($e_i$) with respect to the armchair direction of BP. For the latter method, the BP sample can be rotated under parallel and cross polarization configurations, denoted as $Y(XX)Y$ (parallel polarization) and $Y(XZ)Y$ (cross polarization) or simplified as $XX$ and $XZ$. The corresponding configurations in polarized Raman scattering experiments are shown in **Figure 4**a. Assuming $\theta$ is the angle between the incident polarization and the armchair direction of BP, then $e_i$ and $e_s$ can be written as $e_i = e_s = (\sin\theta, 0, \cos\theta)$ under parallel ($XX$) polarization, by decomposing the incident and scattered polarization vectors with respect to the crystal coordinate system. For the $B_{1g}$ and $B_{3g}$ modes, $I(B_{1g})_{XX/XZ} = I(B_{3g})_{XX/XZ} = |\mathbf{e}_i\mathbf{R}\ \mathbf{e}_s|^2 = 0$, suggesting that $B_{1g}$ and $B_{3g}$ cannot be detected in backscattering configuration. Similarly, $I(A_g)_{XX} = (a\cos^2\theta + c\sin^2\theta)^2$, $I(B_{2g})_{XX} = e^2\sin^2 2\theta$, which indicates that the polarized Raman scattering of BP is dependent on $\theta$, and the $A_g$ modes show the maximum and minimum intensities at $\theta = 0°$ (armchair) or 90° (zigzag), which can be exploited to identify the crystalline orientation of BP (**Table 1**).[16c]

### 4.2. Angle-Resolved Polarized Raman Scattering of BP and Its Controversy in Identifying the Crystalline Orientations

At the very beginning of BP's reintroduction into the 2D material community, two groups (Xia's and Lu's) first reported that the Raman intensities of the three modes ($A_g^1$, $B_{2g}$, and $A_g^2$) in thin BP crystals change significantly with the polarization of the incident light (using method I).[1g,28a] From the perspective of the atomic vibration directions, Lu and co-workers

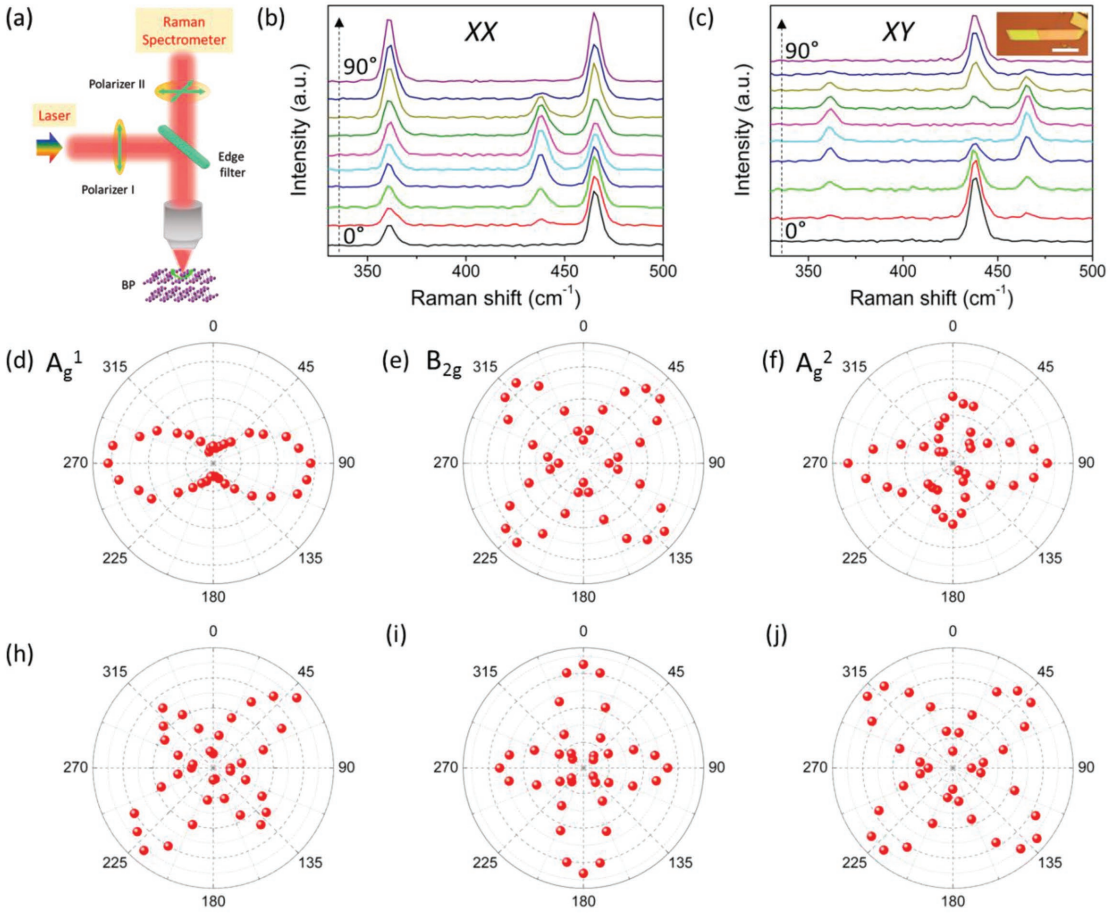


**Figure 4.** a) The experimental diagram of the polarized Raman scattering measurement. Reproduced with permission.[11] Copyright 2016, Wiley-VCH. b,c) Angle-dependent polarized Raman spectra by rotating the sample under parallel (*XX*) and cross (*XZ*) polarization. The inset shows an optical image of a thick BP sample; the scale bar is 10 µm. Polar plots of the polarized Raman intensities of the $A_g^1$, $B_{2g}$, and $A_g^2$ modes under: d–f) parallel and h–j) cross polarization. b–j) Reproduced with permission.[16c] Copyright 2015, Wiley-VCH.

reported that the $A_g^2$ and $B_{2g}$ bands of 15L BP show the maximum and minimum Raman intensities, respectively, when the incident light is polarized along the zigzag direction of BP sample, while the $A_g^1$ mode is not very sensitive to the incident polarization.[28a] However, the conclusion is quite different from the polarization-dependent Raman results by Xia's report.[1g] Almost at the same time, Zhang's group[16c] systematically investigated the polarized Raman scattering of BP by using method II (Figure 4a), which can be widely used to identify the crystalline orientation of BP. As shown in Figure 4b,c, the polarized Raman intensities of the three Raman modes in the thick BP (inset in Figure 4c) change periodically with sample rotation angle under both parallel (*XX*) and cross (*XZ*) polarizations. The intensity polar plots of the $A_g^1$ and $A_g^2$ modes under parallel polarization yield 2-lobed and 4-lobed shapes with the maximum intensities at the rotation angle of 90°. The $B_{2g}$ mode yields 4-lobed shapes with the largest intensities at about 45°, 135°, 225°, and 315° (Figure 4h–j). Combined with the angle-resolved direct-current conductance, it was confirmed that the direction with the largest conductance is in accordance with where the maximum Raman intensity of the $A_g^2$ mode is achieved. Therefore, it was concluded that the $A_g^2$ mode of this BP sample shows the largest Raman intensity under 514.5 nm excitation when the incident light is polarized along the armchair direction of BP. However, as confirmed by transmission electron microscopy, Lu et al. and Ma and co-workers reported that the $A_g^2$ mode of the 8.3 nm thick BP with the excitation of 532 nm laser shows the largest Raman intensity when the incident light or analyzer is polarized along the zigzag direction

**Table 1.** Raman Scattering efficiencies of $A_g$, $B_{1g}$, $B_{2g}$, and $B_{3g}$ modes in BP crystals under different polarization configurations.[16c]

| Polarization configuration | XX[1] | XZ[a)] | Rotate polarizer[b)] |
|---|---|---|---|
| $A_g$ | $(a\sin^2\theta + c\cos^2\theta)^2$ | $(a-c)^2\sin^2\theta\cos^2\theta$ | $a^2\sin^2\alpha + c^2\cos^2\alpha$ |
| $B_{2g}$ | $e^2\sin^2 2\theta$ | $e^2\cos^2 2\theta$ | $e^2$ |
| $B_{1g}$ | 0 | 0 | 0 |
| $B_{3g}$ | 0 | 0 | 0 |

[a)]The configuration of rotating the sample under parallel (*XX*) and cross polarization (*XZ*); [b)]The configuration of rotating the incident polarization without an analyzer.

of BP, which is opposite to the aforementioned reports.[16c,29a] At this point it seems that both of these two methods used to identify the crystalline orientation of BP by polarized Raman scattering are in controversy.[1g,l,5f,11,15a,16c,24b,28a,29,30] In addition, it was further confirmed that the angle-dependent polarized Raman scattering of BP is dependent on the sample thickness, the excitation energy, and the phonon modes.[5d,f,11] As shown in **Table 2**, Ling et al. measured the angle-dependent polarized Raman intensity of BP samples with thicknesses of around 5, 20, 40, and 200 nm under excitation lasers of 532, 633, and 785 nm.[5f] Taking the 20 nm BP sample as an example, the main axes (the direction with the maximum intensity) of the polar plots for both the $A_g^1$ and $A_g^2$ modes vary between armchair and zigzag for different excitation energies. The main axes of the $A_g^2$ mode are at 30° and 120° for 532 and 633 nm excitations, respectively. Under the same excitation energy, the main axes of $A_g^2$ mode also vary with increasing thickness, which are at 30° for 5, 20, and 40 nm thick BP, and 130° for 200 nm thick BP under 532 nm excitation. Apparently, the main axes of the polar plots for $A_g^1$ and $A_g^2$ modes in the 20 nm BP sample are mutually perpendicular under the 532 nm excitation. In this regard, identifying the crystalline orientation of BP using angle-resolved polarized Raman is rather complicated. One should take the thickness of BP, the excitation energy, and the phonon modes into consideration simultaneously in order to figure out the crystalline orientation correctly.

As discussed above, no matter whether the angle-dependent polarized Raman spectra of BP are carried out by rotating the sample under *XX/XZ* polarization or rotating the polarizer, the measured |**a**|/|**c**| values can be used to indicate the main axes of the polar plots. When |**a**| < |**c**|, the largest Raman intensity was observed when the incident light was polarized along the armchair direction of BP under both configurations. However, |**a**|/|**c**| values suffer from the influence of the optical anisotropy of BP, such as the birefringence and linear dichroism effects, anisotropic electron–photon interactions, and electron–phonon interactions in BP. It is also influenced by external factors, such as the interference effect of the substrates and the experimental configurations,[5d,f,11,29b] which will be discussed in the following sections.

**Table 2.** The anisotropic polarized Raman scattering of 5, 20, 40, and 200 nm thick BP under the excitations of 532, 633, and 785 nm lasers. The main axes of the Raman intensity polar plots are indicated by the blue and green arrows. Reproduced with permission.[5f] Copyright 2016, American Chemical Society.

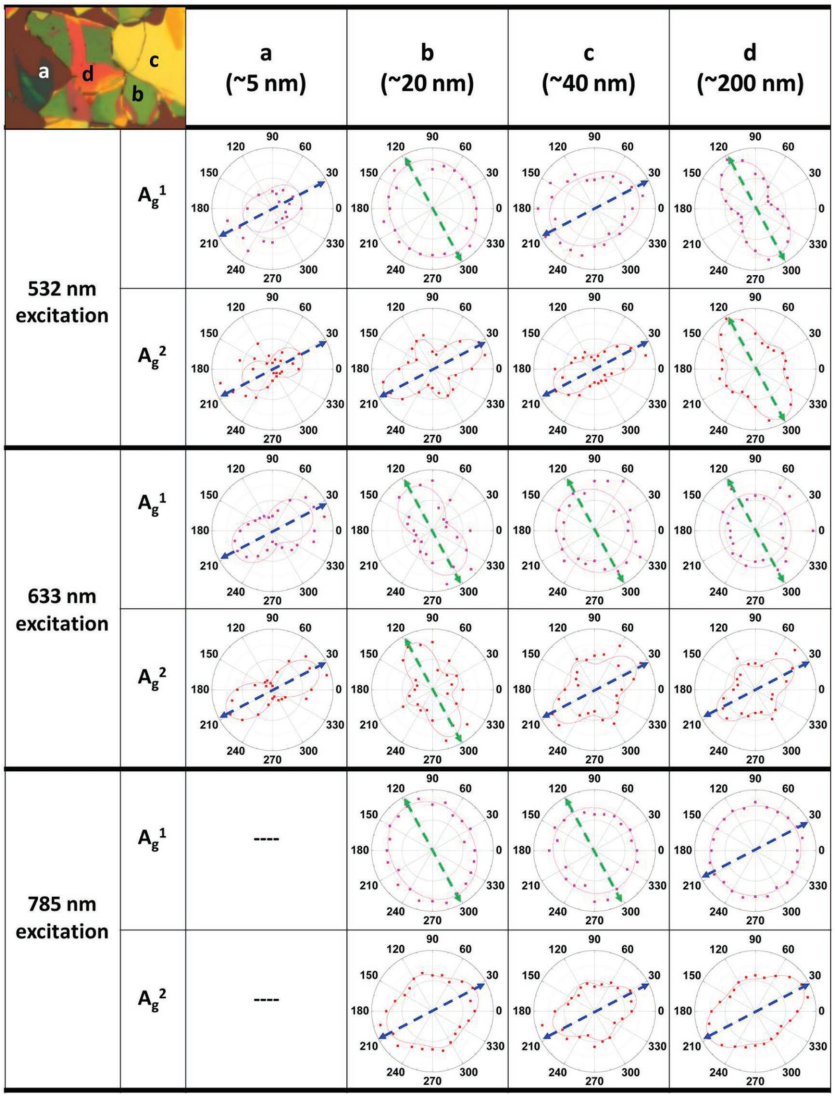


### 4.3. Abnormal Polarized Raman Scattering in BP and Its Dependence on the Excitation Energy, Thickness, and Phonon Modes

Distinguished from isotropic 2D crystals, anisotropic BP crystals present abnormal polarized Raman scattering, which cannot be interpreted by the normal Raman selection rule. As shown in **Figure 5**a–d, the experimental results of the angle-dependent polarized Raman intensities of the totally symmetric $A_g^2$ modes (dots) in BP do not match with the calculated Raman efficiencies (the solid lines) under either 532 nm or 633 nm excitation. In particular, according to the Raman selection rule, only one maximum intensity is expected for the $A_g^2$ mode when the laser is polarized along one of the crystalline orientations, as shown by the solid lines in Figure 5a,c. However, the experimental data show that the $A_g^2$ mode exhibits two local maximum intensities along both of the crystalline orientations ($\theta$ = 90° and 180°). In addition, as shown in Table 2, the abnormal angular dependence of the polarized Raman scattering of BP is further confirmed to be dependent on the sample thickness, the excitation energy, and the phonon modes.[5d,f,11,29b]

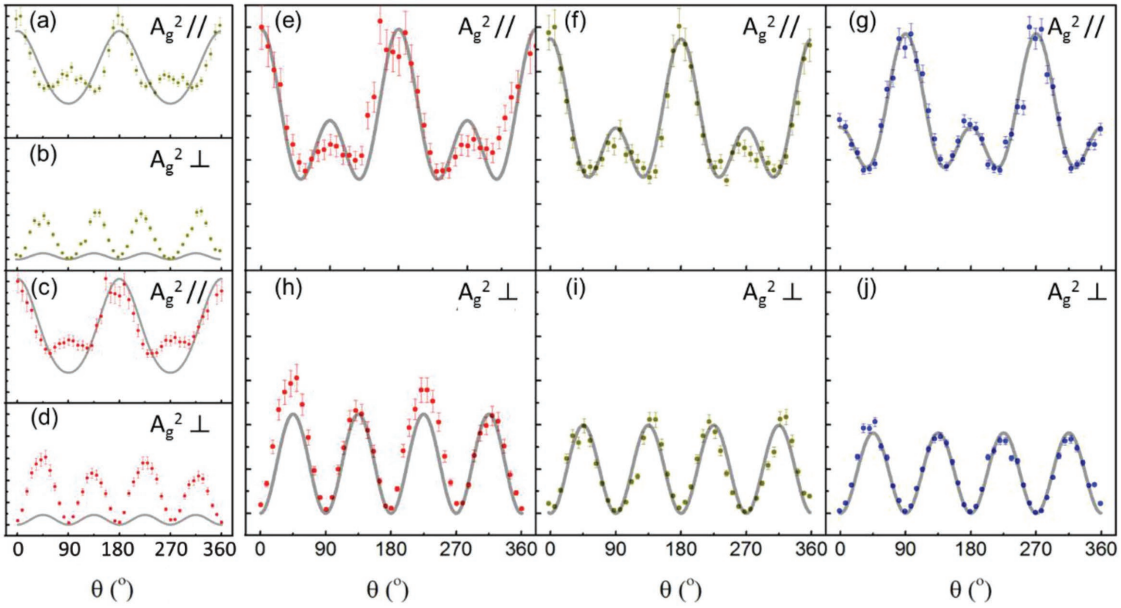


**Figure 5.** a–d) Angle-resolved Raman intensities of $A_g^2$ modes in BP under parallel (//) and cross (⊥) polarization with the excitation wavelength of: a,b) 532 nm and c,d) 633 nm. The solid lines are the best fitting with calculated Raman efficiency. e–j) Angle-resolved Raman intensities of $A_g^2$ modes in BP under parallel (//) and cross (⊥) polarization with the excitation wavelength of 633 nm (e,h), 532 nm (f,i) and 488 nm (g,j). The solid lines are the best fit with the calibrated Raman efficiency based on the complex Raman tensor. a–j) Reproduced with permission.[29b] Copyright 2015, American Chemical Society.

Actually, this phenomenon exists commonly in anisotropic crystals, which dates back to the 1960s.[31] Similar anomalous angle-dependent polarized Raman scattering has been discovered in bulk crystals such as calcite, $LaCl_3$, $YVO_4$, and $NaNO_3$ crystals.[31] It was regarded as the breakdown of the Raman selection rules at the beginning and improper frequency assignments were induced. It was proved later that optical anisotropy is responsible for abnormal angular dependence of bulk anisotropic crystals.[31c,32] Besides anisotropic 2D BP crystals, this abnormal phenomenon also occurred in fully symmetric modes of other 2D family members with low symmetry ranging from orthorhombic to monoclinic to triclinic crystal systems, such as SnSe/SnS, GeS, and $WTe_2$ (orthorhombic); GaTe and 1T' $MoTe_2$ (monoclinic); and $ReS_2$ (triclinic).[33] In the case of BP, the abnormal polarized Raman scattering is mainly attributed to two types of factor. One is the extrinsic factor including the scattering geometry (such as the numerical aperture of the collection lens) and the interference effect of the commonly used 300 nm $SiO_2$/Si substrate. The other stems from the intrinsic property of BP, such as the optical anisotropies (birefringence and linear dichroism effects), anisotropic electron–photon interactions and electron–phonon interactions.[5d,f,11,29b]

Regarding the intrinsic factors, three theoretical models, including two classical theories and one quantum theory, have been applied to explain the abnormal polarized Raman intensities of nonpolar modes in BP crystals and its dependence on the excitation energy, thickness of BP crystals, and different phonon modes.

#### 4.3.1. Complex Raman Tensor

The first reported model based on classical theory takes the complex values of the Raman tensor elements of a phonon mode into consideration.[29b] Since the Raman tensor is described as the derivative of the complex dielectric matrix with respect to the normal coordinates of the crystals, the full expression of Raman tensors should also be complex. In normal cases, only the real part of the Raman tensor element is considered. However, for BP with significant birefringence and anisotropic absorption, the imaginary part should also be taken into consideration.[29b,32b] Hence the Raman tensor of a phonon with $A_g$ symmetry in the orthorhombic BP crystal is

$$\mathbf{R}\left(\mathrm{A_g}\right)=\begin{pmatrix} a\mathrm{e}^{i\varphi_a} & 0 & e \\ 0 & b\mathrm{e}^{i\varphi_b} & 0 \\ e & 0 & c\mathrm{e}^{i\varphi_c} \end{pmatrix} \tag{3}$$

where $a$, $b$, $c$, and $\varphi_a$, $\varphi_b$, and $\varphi_c$ represent the magnitude and complex phase of the three independent components of the tensor, respectively. The calculated intensities of the $A_g$ mode (**Table 3**) match well with the experimental results under parallel and cross polarization configurations with different excitation wavelengths, as shown in Figure 5e–j.[29b]

**Table 3.** Calibrated Raman efficiency of $A_g$ and $B_{2g}$ modes in BP crystals under different polarization configurations.[11,29b]

| Polarization configuration | *XX* | XZ |
|---|---|---|
| $A_g$ | $a^2\sin^4\theta + c^2\cos^4\theta + 2ac\sin^2\theta\cos^2\theta\cos2\varphi_{ac}$ [a)] | $(a-c)^2\sin^2\theta\cos^2\theta$ |
| $B_{2g}$ | $e^2\sin^2 2\theta$ | $e^2\cos^2 2\theta$ |

[a)] $\varphi_{ac}$ refers to the phase difference between $\phi_a$ and $\phi_c$ in the first model.

#### 4.3.2. Birefringence-Directed Raman Selection Rule

In contrast, the second model considers the change of electric field vectors of the incident and scattered light due to the optical birefringence and linear dichroism of the anisotropic crystal.[34] The polarizations of the incident and scattered light involved in the Raman scattering of biaxial BP crystals suffer from the influence of the birefringence and linear dichroism of BP. Therefore, the calibrated electric field vectors of the incoming and scattered light ($\mathbf{e}_i$ and $\mathbf{e}_s$) should be used in the calculation of Raman efficiency. This model explains the experiments as well as the first model. However, here $\varphi_{ac}$, indicated as $\varphi_{ac} = \frac{2\pi}{\lambda}(n_z - n_x)\Delta d$, has a real physical meaning, and represents the phase difference between the two birefringence-induced polarized components.[11] In some sense, this classical model is mathematically equivalent to the first model. However, this model successfully interprets the abnormal angular dependence on the thickness of the BP sample, the excitation energy, and the Raman modes, and perfectly fits the experimental Raman results in **Figure 6**. This is further confirmed by the fact that the fitted phase difference $\varphi_{ac}$ and anisotropy ratio ($|\mathbf{a}|/|\mathbf{c}|$) are dependent on the sample thickness, the excitation energy, and the phonon modes. For example, as shown in Figure 6d,f, the derived phase differences $\varphi_{ac}$ are distinct for the same $A_g^2$ mode in 9.6 nm thick BP sample with an excitation wavelength of 488 nm ($\varphi_{ac} = 42°$) and 633 nm ($\varphi_{ac} = 38°$) as well as the different modes for the same BP sample ($\varphi_{ac}(A_g^1) = 16°$ and $\varphi_{ac}(A_g^2) = 45°$). It can also be seen from Figure 6e that the fitted phase differences of the $A_g^2$ mode are different for the 9.6 and 76 nm thick regions of the same BP sample. Overall, this model provides a quantitative and full understanding of the abnormal angular-dependent Raman scattering of the fully symmetric Raman modes in BP crystals, which can also be extended to the other anisotropic 2D crystals, such as SnSe/SnS, GeS, $WTe_2$, GaTe, 1T' $MoTe_2$, and $ReS_2$.

#### 4.3.3. Anisotropic Photon–Electron Interaction and Phonon–Electron Interaction

Ling et al. provided a qualitative explanation for this anomalous angular Raman dependence from the perspective of the quantum physics.[5f] According to the microscopic Raman theory, the process of first-order Raman scattering for a phonon involves three processes; that is, two photon–electron interaction and one phonon–electron interaction. The probability of the Raman scattering for a given Raman mode is described as[35]

$$P_{\text{Raman}} \propto \left| \sum_{n,n'} \frac{\langle \mathbf{i} | \mathbf{H}_{\text{light}} | \mathbf{n}' \rangle \langle \mathbf{n}' | \mathbf{H}_{\text{el-ph}} | \mathbf{n} \rangle \langle \mathbf{n} | \mathbf{H}_{\text{light}} | \mathbf{f} \rangle}{(E_\lambda - E_{ii})(E_\lambda - E_{ii} - E_{\text{ph}})} \right|^2 \quad (4)$$

where i and f are the initial and the final electronic states of the Raman scattering, respectively. $n'$ and $n$ are the two intermediate states. $E\lambda$, $E_{ii}$, and $E_{\text{ph}}$ are the excitation photon energy, electron–hole transition energy, and phonon energy, respectively. The first term $\langle \mathbf{i}|\mathbf{H}_{\text{light}}|\mathbf{n}'\rangle$ and the third term $\langle \mathbf{n}|\mathbf{H}_{\text{light}}|\mathbf{f}\rangle$ describe the absorption and the emission process of photons, and are related to the electron–photon interaction involved in the Raman scattering. The middle term $\langle \mathbf{n}'|\mathbf{H}_{\text{el-ph}}|\mathbf{n}\rangle$ represents the electron–phonon interaction. As shown in **Figure 7**a, the 9 and 225 nm thick BP absorb more light along the armchair direction than the zigzag direction, indicating the anisotropy of the photon–electron interaction in BP. In addition, the calculated transition probabilities for the allowed optical transition engaged in Raman scattering is dependent on the excitation energy. For instance, with the excitation energies of 0.82 and 4.33 eV, the allowed electron transitions in trilayer BP are $B_{3g} \rightarrow B_{2u}$ and $A_u \rightarrow B_{3g}$, respectively. The former has the largest (smallest) transition probability when the incident light is along the armchair (zigzag) direction, while the latter occurs with the opposite. Therefore, the angle-resolved polarized Raman spectra are strongly dependent on the incident laser energy.

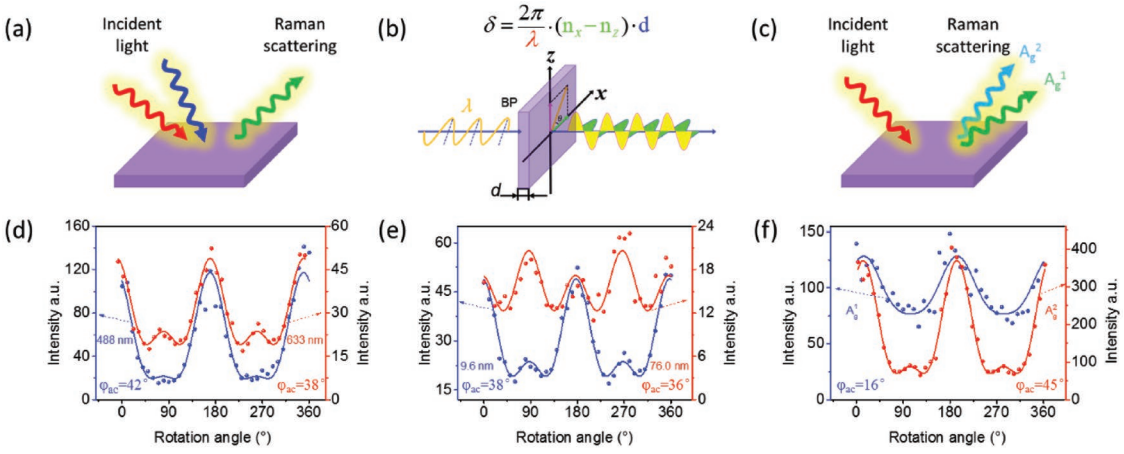


**Figure 6.** Schematic illustration of the influence of a) excitation wavelength, b) thickness, and c) phonon modes to the abnormal polarized Raman of BP in the model of birefringence-directed Raman selection rule. The experimental results of the angle-dependent polarized Raman intensities for the $A_g^1$ and $A_g^2$ modes: d) the $A_g^2$ modes for 70 nm thick BP with the excitation wavelengths of 488 and 633 nm; e) $A_g^2$ modes for 9.6 and 76 nm thick BP with 632.8 nm excitation; f) the $A_g^1$ and $A_g^2$ modes for 9.6 nm thick BP with an excitation laser of 514.5 nm. a–f) Reproduced with permission.[11] Copyright 2016, Wiley-VCH.

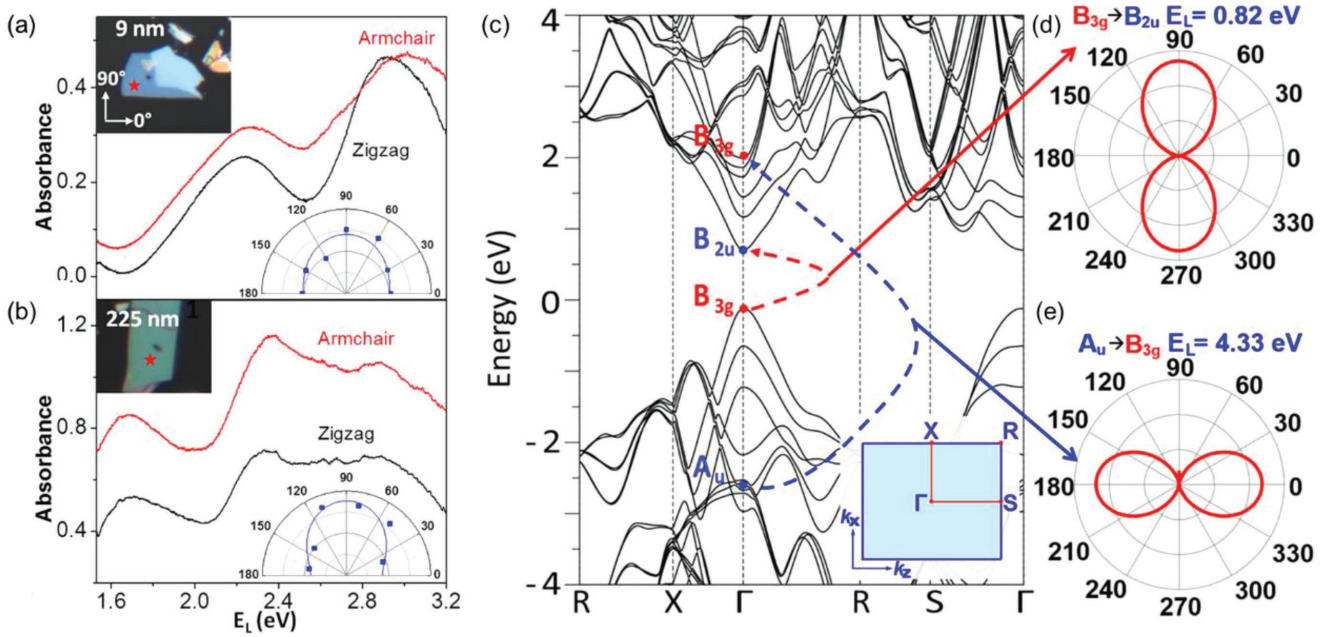


**Figure 7.** a,b) The anisotropic absorbance of the a) 9 nm thick and b) 225 nm thick BP sample. The insets show polar plots of the angle-dependent absorption at 633 nm. c) The calculated band structure of trilayer BP. Inset: 2D Brillouin zone of trilayer BP. d,e) The polar plots of the electron transition probabilities of the first Brillouin zone of bulk BP, from the $B_{3g}$ band to $B_{2u}$ band (d) and from the $A_u$ band to the $B_{3g}$ band (e). a–e) Reproduced with permission.[5f] Copyright 2016, American Chemical Society.

Besides the intrinsic effects of the optical anisotropic nature of BP, the polarized Raman scattering of BP is also affected by extrinsic factors, such as the optical interference of the substrate, the focal length and the collection angle of the lens, the scattering geometry, and crystal alignment.[31d] Considering the optical interference of both the substrate and the BP, Kim et al. has reported that the polarization-dependent enhancement factors of the $A_g$ modes in BP on 300 nm $SiO_2$/Si substrates differ greatly along the armchair and zigzag directions of BP.[5d] Due to the birefringence and linear dichroism effect of BP, the polarized Raman scattering is significantly enhanced along zigzag direction compared to the armchair direction. Through corrections that exclude the interference effect, the polarization dependence of the $A_g$ modes becomes fairly similar for BP samples with different thicknesses (5, 65, 70, and 90 nm). Thus, they claimed that the interference enhancement is the main cause for the thickness-dependent polarized Raman scattering of thin BP. However, it fails to explain the excitation energy dependence.

## 5. Interlayer Shear and Layer Breathing Modes in BP Crystals

Besides the high-frequency intralayer modes related to the strength of chemical bonds, another kind of vibrational mode exists, that involves the relative vibrations of the individual BP layers, either perpendicular or parallel to the layer plane, that is, the interlayer breathing (or compression, labeled as "B" mode) and shear (C) modes,[5c,20,36] which are considered to be rigid-layer Raman modes.[37] These modes are directly related to the interlayer coupling and the sample thickness, and are usually located in the low-frequency region (below 100 $cm^{-1}$) due to the relatively weak interlayer interactions between adjacent layers.[15a] Therefore, the characterization of the interlayer Raman modes can provide essential information to determine the layer number and quantify the interlayer interaction of BP layers.

According to theoretical studies, the low-frequency interlayer phonons in bulk BP are either IR-active or optically inactive, so they cannot be detected in Raman measurements.[36a] These phonons have been studied by inelastic neutron scattering in the 1980s, and it was found that there is one B mode located at ≈87 $cm^{-1}$ and two C modes at 19 $cm^{-1}$ ($C_x$, vibrating along the armchair direction) and 52 $cm^{-1}$ ($C_y$, vibrating along the zigzag direction).[12b] Different from other 2D layered materials (graphene, TMDs), $C_x$ and $C_y$ are nondegenerate due to the in-plane anisotropic structure of BP.[12b] Compared to the bulk phase, the lattice symmetry of few-layer BP is reduced due to its limited translational symmetry in the *z*-direction, so the optical activity of the phonon modes changes; that is, some Raman inactive modes in the bulk phase become Raman active in few-layer samples.[38] Although bulk BP and *N*-layer (*NL*) BP belong to different space groups, they all belong to the same point group $D_{2h}$ so their Raman modes have the same symmetry classifications and the same forms of Raman tensors regardless of the sample thicknesses. Group theory analysis suggests that even *N*L BP has $N/2$ Raman active B modes ($A_g$) and $N$ Raman active C modes ($B_{1g}$ or $B_{3g}$), whereas odd *N*L BP has $(N-1)/2$ B modes and $N-1$ C modes.[15a] Based on the calculation formula for the Raman scattering efficiency, $B_{1g}$ and $B_{3g}$ modes can only be detected when the incident light has the component polarized along the *z*-direction; in other words, the C mode cannot be observed under back-scattering configuration for the few layer BP sheet. On the other hand, interlayer vibrational phonons do not exist in monolayer BP flakes. Therefore, only

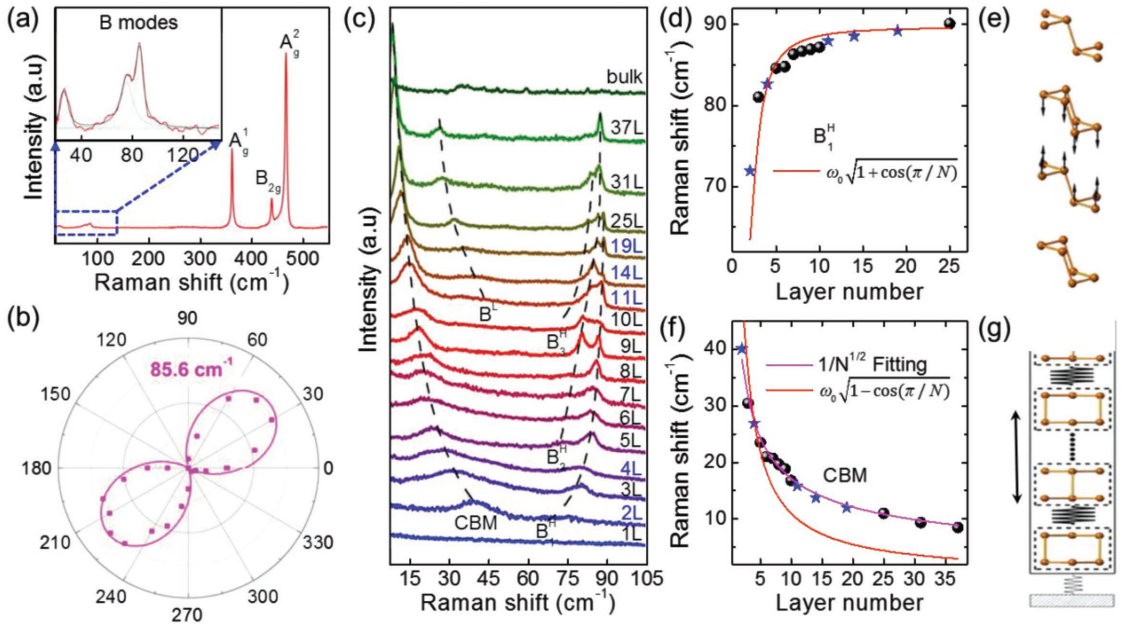


**Figure 8.** a) Interlayer vibrations in Raman spectrum of a few-layer BP flake; the inset shows the zoomed-in spectrum in the frequency range of 20–150 $cm^{-1}$. b) Polarization dependence of the highest-frequency interlayer breathing mode for this sample. a,b) Reproduced with permission.[15a] Copyright 2015, American Chemical Society. c) Raman spectra for BP samples with different thickness. CBM denotes the collective breathing mode, and $B_n^H$ ($B_n^L$) denotes the *n*th-order breathing mode from the higher (lower) branch. d–g) Layer number dependence of: d) CBM and f) $B_1^H$ modes and e,g) the corresponding vibration patterns. The pink and red solid lines in (d) and (f) are the fitting curves by $1/N^{1/2}$ and linear chain model. c–g) Reproduced with permission.[37a] Copyright 2016, American Physical Society.

the B mode can be observed in the Raman spectra of *N*L ($N \geq 1$) BP samples under the condition of normal incidence.[38] Moreover, the B mode in few-layer BP should be located at a lower frequency than that in the bulk phase (≤87 $cm^{-1}$).

As shown in **Figure 8**a, except the three high-frequency intralayer Raman peaks ($A_g^1$, $B_{2g}$, and $A_g^2$), the three B modes (zoomed-in spectrum in the inset) lying around 26.2, 75.6, and 85.6 $cm^{-1}$ can be observed in the Raman spectrum of this few-layer BP sample (layer number larger than 6), which are about two orders of magnitude weaker than that of the high-frequency modes.[15a] Based on the scattering-efficiency analysis of the $A_g$ mode in the previous section, the intensities of the B modes depend on the crystalline orientation of the BP sample relative to the polarization direction of the incident light. As shown in Figure 8b, the B mode, lying at 85.6 $cm^{-1}$, exhibits a 180° variation period with the sample rotation angle under a parallel polarization configuration. The other two B modes located at 26.2 and 75.6 $cm^{-1}$, also show a similar polarization dependence. All of them reach the maximum and minimum intensities at 45° (or 225°) and 135° (or 315°), corresponding to the armchair or zigzag direction of the BP sheet. For this sample, the armchair axis is oriented along the 45° direction. It is important to point out that different B modes show different ratios of maximum-to-minimum intensity, even though they have the same symmetry. This is because the values of the $c/a$ ratio in the Raman tensors are different.

As mentioned above, the number of B modes is dependent on the thickness of the BP samples not only for even *N*L samples but also for odd *N*L samples.[37a] Figure 8c shows the Raman spectra of BP samples with different thicknesses. It can be seen that both the frequencies and widths of the low-frequency Raman peaks change with the thickness, which can be used to accurately determine the layer number of BP samples, and there are no low-frequency modes for single-layer and bulk BP. Two types of Raman modes, CBM (collective breathing mode) and $B^H$ modes (H represents high frequency), with opposite thickness dependence can be observed in the Raman spectra. The $B^H$ mode shifts to higher frequency as the layer number increases ($B_1^H$ lying at ≈71 $cm^{-1}$ in bilayer BP and ≈90 $cm^{-1}$ in multilayer sample), while the CBM shifts to lower frequency with increasing sample thickness (lying at ≈40 $cm^{-1}$ in bilayer and ≈8 $cm^{-1}$ in multilayer flake). Another $B^H$ mode appears when the layer number increases to five, and three $B^H$ modes exist when the sample is thicker than ten layers. In addition, another B mode (labeled as $B^L$, where L represents low frequency) can be observed for similar thickness-dependent frequencies as in the CBM case when the layer number is larger than 11. On the other hand, all of the B modes (including CBM, $B^L$, and $B^H$ modes) become sharper as the layer number increases, that is, the peak widths decrease.

The standard linear-chain model is used to describe the quantitative relationship between the frequency of the interlayer Raman modes (B and C modes) and the number of layers. The interlayer coupling in other layered materials can also be derived from this relationship.[39] The frequency of the B mode and the layer number have the following relationship: $\omega = \omega_0 \sqrt{1 \pm (\pi / n)}$,[37a,39a] where $\omega$ is the frequency of the B mode and $N$ is the layer number. $\omega_0$ is the Raman shift of the B mode in a bilayer sample, and can be expressed as $\omega_0 = (1/(\sqrt{2}\pi c))\sqrt{\alpha/\mu}$, where $c$ is speed of light in vacuum, $\alpha$ is interlayer force constant, and $\mu$ = 1.42 × $10^{-26}$ kg $Å^{-2}$ is

the mass per unit area.[37a] The fitting of the $B_1^H$ branch using the above relationship is illustrated in Figure 8d. The interlayer force constant can be obtained from the fitting result: $\alpha = 1.27 \times 10^{20}$ N m$^{-3}$, which is several times larger than that in graphene and $MoS_2$, suggesting a stronger interlayer coupling in BP. However, the CBM clearly deviates from the linear-chain model, which is proportional to $1/\sqrt{N}$. This is because the CBM originates from the relative motion between the entire $N$ layers and the substrate, indicating that the interlayer coupling between BP layers is strong enough so that all the BP layers can be coupled together. Therefore, only the B modes ($B^L$ and $B^H$) indeed come from the relative vibration between BP layers, which is generally defined as the breathing mode in layered materials.

Although the number of B modes is linearly proportional to the layer number for both even and odd $N$L BP samples, not all the B modes can be detected and distinguished due to the weak intensity and the small spacing between peak positions. Further work should be carried out to study the B modes in BP samples in detail by improving the spectral resolution of the Raman spectrometer and enhancing the Raman efficiency in the low-frequency region. In addition, studies of the C modes are still limited to theoretical calculations. It is imperative to optimize the light path so that the incident light has the component polarized along $z$-direction to excite the C modes. In a word, systematic studies on the interlayer phonon modes of BP are beneficial to better understand the interlayer coupling, which affect the electronic and mechanical properties of BP.

## 6. Edge Phonons in BP

The edges of 2D crystals usually yield singular optical, electronic, and magnetic properties, which are dramatically different from those deep in the basal plane. Similar to graphene and TMDs, BP presents two types of crystallographic edges, the armchair and zigzag edges (Figure 1c). Previous experimental and theoretical reports have demonstrated that BP edges show outstanding optical, mechanical, and magnetic properties, such as edge plasmons and large room-temperature edge ferromagnetism in the oxidized state, and the edge types will also have significant influence on the bandgap of BP nanoribbons.[40] Therefore, it is crucial to develop approaches to identify the different edge types and probe the peculiar edge-sensitive properties.

Due to the broken symmetry at the edges, the Raman selection rule of the edge phonons is distinct from that in the basal plane, giving rise to new Raman bands. This allows Raman spectroscopy to investigate the edges of 2D layered crystal. Ribeiro et al. studied the edge phonons in exfoliated BP by polarized Raman scattering and discovered that for a 300 nm thick rectangular BP sample, it mainly shows the totally symmetric $A_g^1$ and $A_g^2$ Raman modes under parallel ($XX/ZZ$) configuration and a strong $B_{2g}$ peak under cross ($XZ$) polarization (**Figure 9**a,b).[11] Here, the notations $XX/ZZ$ ($XZ$) refer to the incident light polarized along the armchair ($X/Z$) direction and with the detection polarization along armchair ($X$) or zigzag ($Z$) directions. However, when it is detected on the armchair edge of the BP flake under $XX$ polarization configuration, the $B_{2g}$ mode becomes stronger, and two additional peaks, assigned as $B_{1g}$ (190 cm$^{-1}$) and $B_{3g}^1$ (230 cm$^{-1}$) modes, emerge in the Raman spectrum. According to the Raman selection rule, as discussed in previous sections, these two modes are not allowed in the backscattering configuration, due to the zero $xz$ and $zx$ component of the corresponding Raman tensor. The edge phonons also show the unique Raman selection rule. For example, as shown in Figure 9d, the $A_g^1$ and $A_g^2$ modes show higher intensity at zigzag and armchair edges, respectively, in the $XZ$ polarization configuration. The $B_{2g}$ modes can be clearly observed at the armchair edge

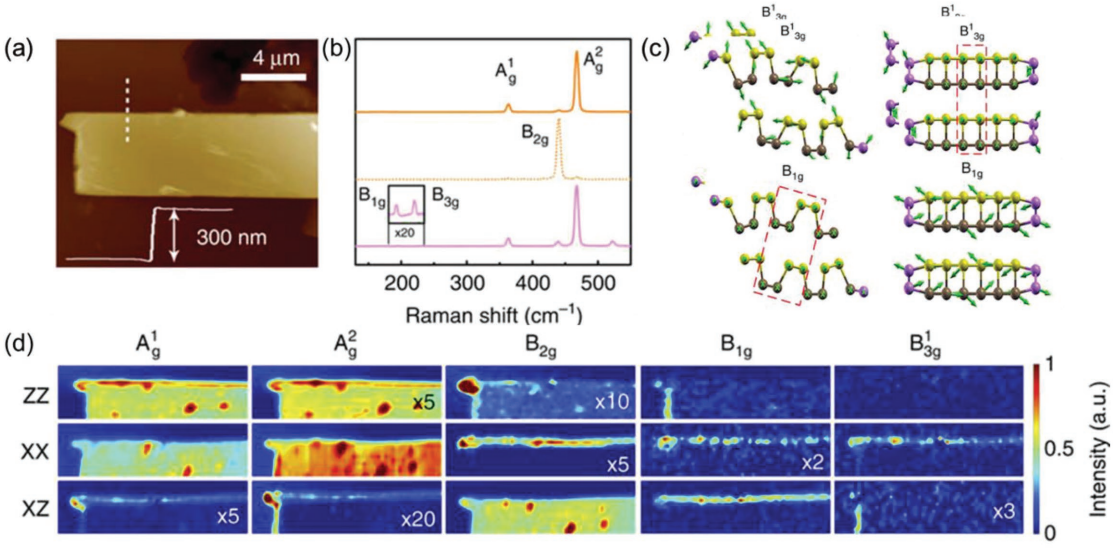


**Figure 9.** a) Atomic force microscopy (AFM) image of the exfoliated BP flake. b) Raman spectra of BP in the center region under parallel ($XX$) and cross ($XZ$) polarization configuration and at the armchair edge with parallel ($XX$) polarization. The inset shows the zoom-in spectrum of the $B_{3g}^1$ and $B_{1g}$ modes. c) The atomic displacement of the $B_{3g}^1$ and $B_{1g}$ modes at the zigzag (left) and armchair (right) edges. The edge atoms are marked with purple. d) Raman mapping images of different Raman modes $A_g^1$, $A_g^2$, $B_{2g}$, $B_{1g}$, and $B_{3g}^1$ under three different polarization configuration ($ZZ$, $XX$, and $XZ$). a–d) Reproduced with permission.[11] Copyright 2016, Nature Publishing Group.

in the *ZZ* polarization configuration and at the zigzag edge in the *XX* configuration. In addition, the $B_{1g}$ edge phonon appears at the zigzag edge in the *ZZ* polarization condition and armchair edge in both the *XX* and the *XZ* configurations, whereas the $B_{3g}^1$ mode is not visible in the *ZZ* configuration, while it appears at zigzag edge in the *XX* configuration and at armchair direction in the *XZ* polarization configuration.[1l] The different behavior of the edge phonon in BP is attributed to the edge-reconstruction-induced distinct atomic displacement at the edges. The edge atoms within the same puckered layer move closer together in the relaxed armchair edge, while the zigzag edge displays stretching and contraction of the puckered structure. Figure 9c shows the corresponding atomic displacement of the $B_{3g}^1$ and $B_{1g}$ phonons at the zigzag (left) and armchair (right) edges. Similar edge phonons are also observed in $MoO_3$ crystals.[41]

## 7. Raman Scattering of BP under External Perturbation: Temperature, Pressure, and Strain

The Raman scattering of BP is quite sensitive to changes of the external perturbations, such as temperature, pressure, and strain. The investigation of Raman scattering in BP under external perturbations is important both to gain insight into their fundamental thermal and mechanical properties and for their applications in sensing the external perturbations.

### 7.1. Temperature

The study of the temperature-dependent Raman scattering of few-layer BP is important to further understand its thermal property.[28,42] The measured Raman shifts versus temperature can be characterized by a linear equation: $\omega = \omega_0 + \chi T$, where $\omega_0$ is the phonon frequency at 0 K and $\chi$ is the first-order temperature coefficient.[28,42a–c] Late studied the temperature-dependent Raman spectra of a few-layer BP sample, which depicts softening of the $A_g^1$,$B_{2g}$, and $A_g^2$ modes with temperature increasing from 77 to 673 K. The results are shown in **Figure 10**, where the measured coefficients $\chi$ of three characteristic Raman modes are –0.008, –0.013, and –0.014 $cm^{-1}$ $K^{-1}$.[42a] Other reports in the literature have also detailed similar temperature-dependent softening phenomena.[28,42b–d] However, the temperature coefficients are slightly different due to diverse measurement conditions, including the sample thickness, the laser polarization, the range of temperature, and the local surroundings of the material.[28,42a–d] Typical experimental configurations and results are summarized in **Table 4**. The observed softening of Raman modes is attributed to the anharmonic phonon coupling and especially large lattice thermal expansion as found in graphene.[28b,43] The temperature coefficients of few-layer BP are comparable to that of graphene (–0.0154 $cm^{-1}$ $K^{-1}$ for the G band)[44] and $MoS_2$ (–0.0123 and –0.0132 $cm^{-1}$ $K^{-1}$ for the $A_{1g}$ and $E_{2g}^1$ modes).[45] The thermal effect on the Raman scattering of few-layer BP on hafnium dioxide ($HfO_2$) high-$\kappa$ dielectric has also been reported.[42e] With an annealing temperature up to 200 °C, the BP film exhibits blueshifts in both the out-of-plane ($A_g^1$) and in-plane ($B_{2g}$ and $A_g^2$) modes. With increasing temperature, the additional thermal energy is found to promote the relaxation of strain in the sample, resulting in a distortion of the film crystallinity.[42e] In turn, the thermal-effect-induced frequency shift for the Raman modes in BP have been exploited to determine the anisotropic thermal conductivities of BP, which are ≈20 and ≈40 W $m^{-1}$ $K^{-1}$ along the armchair and zigzag direction of BP film thicker than 15 nm.[28b]

Besides the frequency shift, the full-width at half-maximum (FWHM) of the Raman modes also gets broader with increasing temperature.[42a–d] This phenomenon is ascribed to the electron–phonon/phonon–phonon interaction and

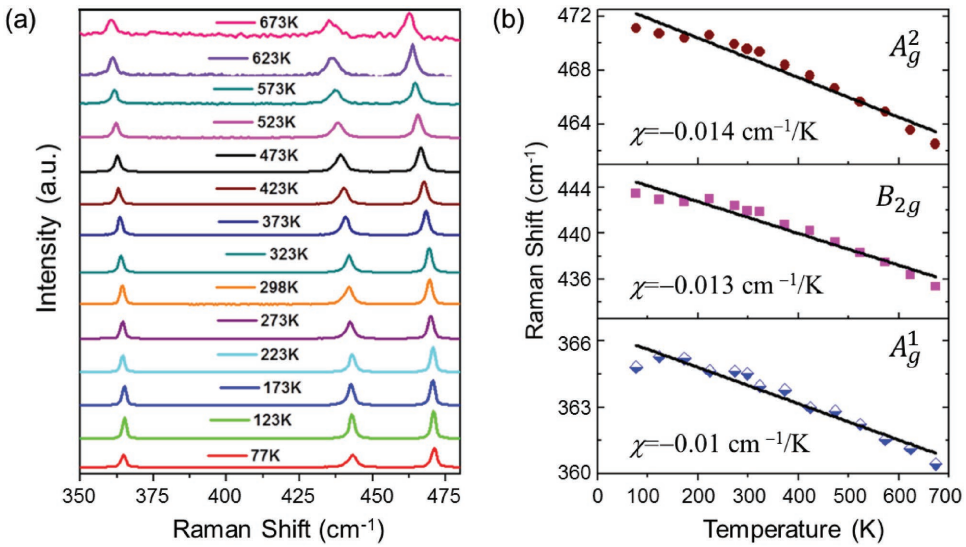


**Figure 10.** a) Raman spectra of the few-layer BP sample in a temperature range of 77–673 K. b) Temperature dependence of $A_g^1$, $B_{2g}$, and $A_g^2$ modes of a five-layer BP between 103 and 293 K. a,b) Reproduced with permission.[42a] Copyright 2015, American Chemical Society.

**Table 4.** The temperature coefficients $\chi$ of $A_g^1$, $B_{2g}$, and $A_g^2$ modes under different experimental configurations.

| Experimental configuration[a)] | Temperature coefficient [$cm^{-1}$ $K^{-1}$] | | | References |
|---|---|---|---|---|
| | $A_g^1$ | $B_{2g}$ | $A_g^1$ | |
| S ($SiO_2$/Si), *d* (≈4 nm), TR (77–673 K) | –0.008 | –0.013 | –0.014 | [42a] |
| S ($SiO_2$/Si), *d* (≈3.2 nm), TR (113–293 K) | –0.023 | –0.018 | –0.023 | [28a] |
| Suspended, *d* (≈9.5 nm), TR (296–345 K) | –0.019 | –0.025 | –0.023 | [28b] |
| Suspended, *d* (≈9.5 nm), TR (296–345 K) | –0.022 | –0.029 | –0.027 | [28b] |
| S ($SiO_2$/Si), *d* (≈6 nm), TR (250–400 K) | –0.016 | –0.027 | –0.028 | [42b] |
| S ($SiO_2$/Si), *d* (≈9.5 nm), TR (250–400 K) | –0.017 | –0.028 | –0.028 | [42b] |
| S (Si), *d* (≈10 nm), TR (78–573 K) | –0.028 | –0.028 | –0.018 | [42c] |
| Suspended, *d* (≈70 nm), TR (298–598 K) | –0.022 | –0.034 | –0.035 | [5h] |
| S ($SiO_2$/Si), *d* (≈70 nm), TR (298–598 K) | –0.019 | –0.031 | –0.032 | [5h] |

[a)]The laser is polarized in parallel to the zigzag or armchair axes of BP; *s* is the sample thickness, TR is the temperature range, and S is the supported substrate.

anharmonic terms, and can be explained by using double-resonance theory.[42a,c,46]

### 7.2. Pressure

Pressure has been used to change the structure and modify the electronic structures and vibrational features of BP.[13,47] Theoretical and experimental studies have showed that there are three important transition points ($P_1$, $P_2$, and $P_3$) to BP samples with increasing pressure, and high-pressure Raman spectroscopy has been proven to be a sensitive tool to characterize these transitions.[47a,48] As shown in **Figure 11**, the first turning point is an electronic topological transition at $P_1 \approx 1.1$ GPa, meaning that BP would become a 3D Dirac semimetal from a direct-gap semiconductor due to the band crossover near the Z point in the Brillouin zone with linear dispersion, and the FWHM of the Raman modes goes through a minimum at $P_1$ due to the effect of electron–phonon coupling.[47] Furthermore, two new Raman modes labeled as N1 and N2 at 240 and 300 $cm^{-1}$ emerge at $P_2 \approx 4.6$ GPa, which means that the BP crystal changes from a layered orthorhombic structure to a rhombohedral structure.[48a] All these three modes of the orthorhombic phase ($A_g^1$, $B_{2g}$, and $A_g^2$) persist even above 4.6 GPa, which may be because the orthorhombic to rhombohedral transformation is not completed at 4.6 GPa. These three typical Raman modes of the orthorhombic structure vanish above $P_3 \approx 11$ GPa, and the structure is transformed to a simple cubic phase. The modes labeled as N1, N2, and N3 observed in the rhombohedral phase have been assigned as $E_g^1$, $A_{1g}$, and $E_g^2$ modes by first-principles analysis. Therefore, the changes in the pressure coefficients of the Raman frequencies, as well as the appearance and disappearance of Raman modes, confirm the electronic and structural transitions of BP.[48a]

### 7.3. Strain

2D crystals have shown outstanding mechanical resilience under elastic strain, much better than conventional bulk materials.[49] It has been found that monolayer BP can withstand a tensile stress and strain up to 10 N $m^{-1}$ and 30%, so BP has been considered as a promising candidate for future flexible electronics.[50] The strain effects on the electronic, optical, and thermal properties of BP layers have attracted great attention in recent years,[49c,51] such as direct-to-indirect bandgap transition, semiconducting-to-metal transition,[51a] remarkable shift of the optical absorption band-edge between the strained ripples,[49c] and inverse funnel effects of excitons.[51c]

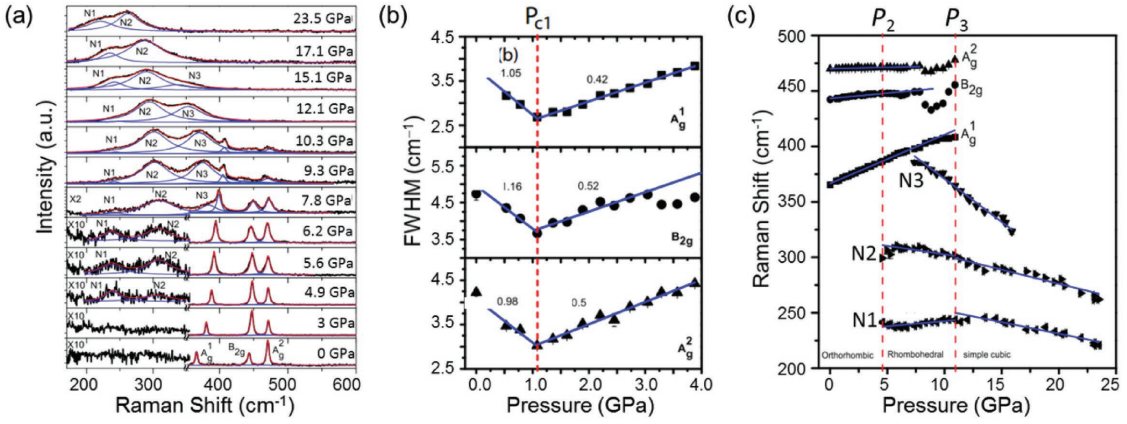


**Figure 11.** a) Pressure evolution of Raman spectra, where N1, N2, and N3 are the new modes. b) Pressure evolution of FWHM of three typical Raman modes in the range 0–4 GPa; the vertical dashed line indicates the transition pressures of semiconductor to topological insulator phase. c) Pressure dependence of the Raman shifts; the vertical dashed lines indicate the two structural phase-transition pressures. a–c) Reproduced with permission.[48a] Copyright 2017, American Physical Society.

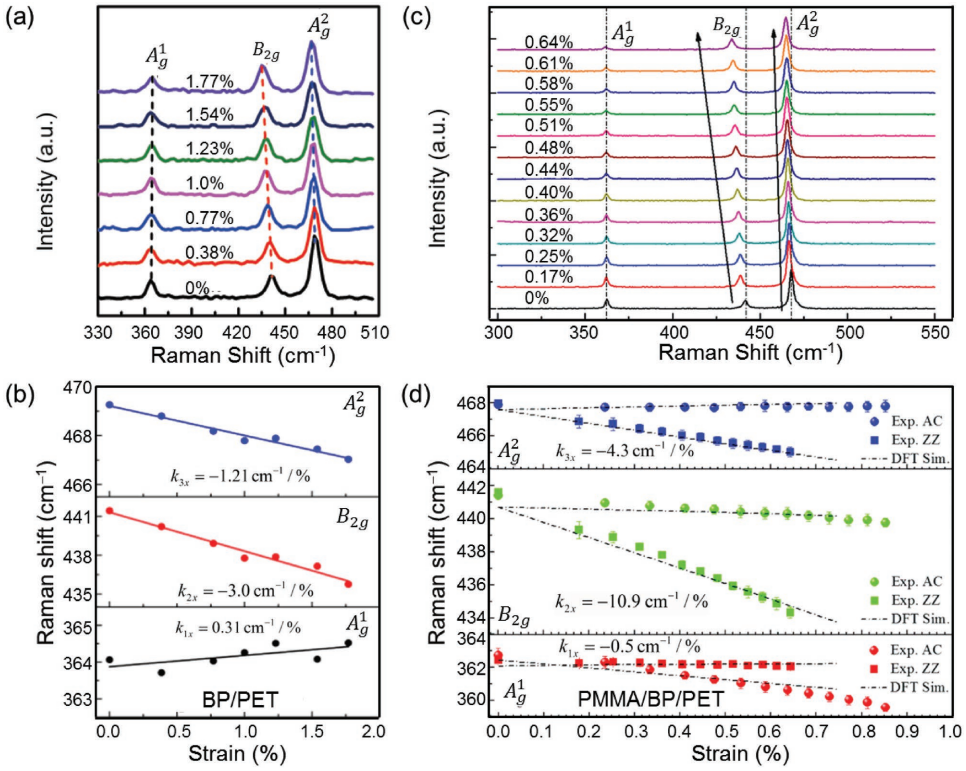


**Figure 12.** a) Raman spectra evolution and b) the fitted Raman shifts of the $A_g^1$, $B_{2g}$, and $A_g^2$ modes of BP as a function of increasing zigzag strain for BP/PET set-up. a,b) Reproduced with permission[17a] Copyright 2017, Wiley-VCH. c) Raman spectra evolution and d) the fitted Raman shifts of $A_g^1$, $B_{2g}$, and $A_g^2$ modes of BP as a function of increasing zigzag strain for PMMA/BP/PET experimental set-up. c,d) Reproduced with permission.[52b] Copyright 2017, Wiley-VCH.

The strain effects on the Raman spectra of ultrathin BP have been investigated in both theory and experiment.[18,52] For anisotropic BP, the changes in the Raman shifts under in-plane uniaxial strain are angle-dependent, and they can be expressed as a combination of the Raman responses under zigzag and armchair strain. In experiments, BP thin films are usually transferred onto flexible polymer substrates in order to apply strain. The strain applied to BP samples was assumed to be the same as the strain applied to the flexible substrate under an ideal approximation.[52,53] However, in many cases, the actual strain applied to BP may be less because of possible interfacial slippage,[49c,54] so the strain-dependent Raman shifts are more susceptible to the experimental set-ups. If a BP flake is transferred onto a poly(ethylene terephthalate) (PET) substrate directly, the absolute change rates of Raman shift versus strain are smaller than 3 $cm^{-1}$ per%,[17a,55] and the maximum rate is from the $B_{2g}$ mode under strain along zigzag direction, as shown in **Figure 12**a,b.[17a] If the BP flake is sandwiched by a poly(methyl methacrylate) (PMMA) layer on the top and a PET substrate (PMMA/BP/PET) at the bottom, the same mode can reach a remarkable redshift rate of 11 $cm^{-1}$ per% (Figure 12c,d).[52b] The large difference of the change rates of Raman shifts under strain is attributed to the different strain transfer efficiencies between substrates and BP samples in the different experimental set-ups. The transfer efficiency of strain can be estimated theoretically through the rate of the peak shift, as reported by Zhang et al.[17a] According to their calculations, only 20 to 40% of the strain was effectively transferred from a PET substrate to a BP flake for direct BP/PET setups. They also reported that the different rates of the three characteristic Raman modes can also be used to identify the relative angle $\theta$ between strain and the zigzag axis of BP[17a]

$$\theta = \begin{cases} 0^\circ & (\text{if } b < 0) \\ 90^\circ & (\text{if } a < 0) \\ \arccos\sqrt{\dfrac{a}{a+b}} & (\text{if } a > 0 \text{ and } b > 0) \end{cases} \tag{5}$$

where $a$ and $b$ are directly related to the experimental change rates $k$ of $A_g^1$, $B_{2g}$, and $A_g^2$ modes

$$\begin{cases} a = 0.0129k_1\left(A_g^1\right) - 0.088k_2\left(B_{2g}\right) - 0.0491k_3\left(A_g^2\right) \\ b = -0.2785k_1\left(A_g^1\right) + 0.0104k_2\left(B_{2g}\right) + 0.0557k_3\left(A_g^2\right) \end{cases} \tag{6}$$

Based on these formulas, the strain angle $\theta$ and the crystalline orientation can be readily determined by the Raman frequency shifts, which is less affected by experimental conditions, such as laser polarization, excitation wavelength, the sample thickness, and the substrate.

## 8. Summary and Outlook

Due to its superior electronic/optical properties and in-plane structural anisotropy, BP has attracted immense attention in the past few years. Raman spectroscopy is an important tool to probe the structural information and study electron–photon and electron–phonon interactions. On the other hand, the unique structural feature of BP provides an opportunity to enrich fundamental information on Raman scattering; in particular, the Raman tensors and Raman selection rules. Here, we have reviewed the recent advances in the Raman scattering of 2D BP crystals, from the basic concept of the crystal symmetry and phonon mode assignments to the characteristic Raman features of BP, including layer-number-dependence, interlayer shear, and layer breathing modes, edge phonons, and the effects of perturbation, such as temperature, strain, and pressure. The deviation from the normal Raman selection rule due to the optical anisotropy, the anisotropic electron–photon and electron–phonon interactions of BP and the modified Raman selection rule have also been discussed. For the future Raman scattering investigation of anisotropic BP, the following aspects should be addressed in more detail.

First of all, it is still an open question as to how the Raman tensors of BP are dependent on the sample thickness, incident laser wavelength, and local surroundings. Due to the weak interlayer interaction between the lamellar structure, the electronic structures of few layer (1–5L) BP strikingly differ from each other. The 2D layered feature of BP allows a quantitative investigation of the layer-number dependence of the Raman tensors. By combining the choice of different lasers, the anisotropic electron–photon and electron–phonon interactions and how they affect the Raman tensors can be further studied. In addition, the anisotropic optical properties such as the birefringence effect, the linear dichroism effect, and the interference effect of the substrate will affect the apparent Raman tensor elements of layered BP.

Furthermore, it is challenging to investigate how the Raman selection rules for BP, as well as other anisotropic 2D materials, are quantitatively modified by the optical anisotropy and anisotropic electron–photon and electron–phonon interactions. Although several models have been established to explain the abnormal Raman selection rules, several aspects are still not clear. For example, even if both the birefringence effect and the interference effect are fully considered, the excitation-energy dependence of Raman scattering of BP is still not fully understood. In addition, the phase difference for the 9.6 nm thick BP fitted by the birefringence-directed Raman selection model does not agree well with the measured results. With this question yet to being answered and quantitatively analyzed, the anomalous Raman selection rules should be better understood, probably with a universal model with enriched insights in terms of the low-dimensional light–matter interactions and the anisotropic electron–phonon interactions. This is crucial for polarized Raman scattering studies of not only BP but also other 2D crystals with low symmetry.

## Acknowledgements

The authors thank Cosmi Yuxuan Lin and Marek Hempel from Massachusetts Institute of Technology for helpful discussions and revisions for this review. This work was financially supported by the National Natural Science Foundation of China (NSFC) (Grant Nos. 21233001, 21790052, 51720105003, 11374355, and 21573004), the Ministry of Science and Technology (MOST) (Grant Nos. 2016YFA0200101, 2016YFA0200104, and 2015CB932400), and the Beijing Municipal Science and Technology Planning Project (Grant No. Z161100002116026).

## Conflict of Interest

The authors declare no conflict of interest.

## Keywords

anisotropic electron–photon interactions, black phosphorus, electron–phonon interactions, Raman scattering, Raman selection rule

Received: December 20, 2017
Revised: January 11, 2018
Published online: April 19, 2018

[1] a) M. Buscema, D. J. Groenendijk, S. I. Blanter, G. A. Steele, H. S. J. van der Zant, A. Castellanos-Gomez, *Nano Lett.* **2014**, *14*, 3347; b) L. K. Li, Y. J. Yu, G. J. Ye, Q. Q. Ge, X. D. Ou, H. Wu, D. L. Feng, X. H. Chen, Y. B. Zhang, *Nat. Nanotechnol.* **2014**, *9*, 372; c) W. Lu, H. Nan, J. Hong, Y. Chen, C. Zhu, Z. Liang, X. Ma, Z. Ni, C. Jin, Z. Zhang, *Nano Res.* **2014**, *7*, 853; d) J. Qiao, X. Kong, Z.-X. Hu, F. Yang, W. Ji, *Nat. Commun.* **2014**, *5*, 4475; e) G. Qin, Q.-B. Yan, Z. Qin, S.-Y. Yue, H.-J. Cui, Q.-R. Zheng, G. Su, *Sci. Rep.* **2014**, *4*, 6946; f) V. Tran, R. Soklaski, Y. F. Liang, L. Yang, *Phys. Rev. B* **2014**, *89*, 235319; g) F. Xia, H. Wang, Y. Jia, *Nat. Commun.* **2014**, *5*, 4458; h) J. Kim, S. S. Baik, S. H. Ryu, Y. Sohn, S. Park, B.-G. Park, J. Denlinger, Y. Yi, H. J. Choi, K. S. Kim, *Science* **2015**, *349*, 723; i) N. Youngblood, C. Chen, S. J. Koester, M. Li, *Nat. Photonics* **2015**, *9*, 247; j) H. Yuan, X. Liu, F. Afshinmanesh, W. Li, G. Xu, J. Sun, B. Lian, A. G. Curto, G. Ye, Y. Hikita, Z. Shen, S.-C. Zhang, X. Chen, M. Brongersma, H. Y. Hwang, Y. Cui, *Nat. Nanotechnol.* **2015**, *10*, 707; k) N. Mao, J. Tang, L. Xie, J. Wu, B. Han, J. Lin, S. Deng, W. Ji, H. Xu, K. Liu, L. Tong, J. Zhang, *J. Am. Chem. Soc.* **2016**, *138*, 300; l) H. B. Ribeiro, C. E. P. Villegas, D. A. Bahamon, D. Muraca, A. H. Castro Neto, E. A. T. de Souza, A. R. Rocha, M. A. Pimenta, C. J. S. de Matos, *Nat. Commun.* **2016**, *7*, 12191; m) L. Li, J. Kim, C. Jin, G. J. Ye, D. Y. Qiu, F. H. da Jornada, Z. Shi, L. Chen, Z. Zhang, F. Yang, K. Watanabe, T. Taniguchi, W. Ren, S. G. Louie, X. H. Chen, Y. Zhang, F. Wang, *Nat. Nanotechnol.* **2017**, *12*, 21; n) G. Zhang, S. Huang, A. Chaves, C. Song, V. O. Özçelik, T. Low, H. Yan, *Nat. Commun.* **2017**, *8*, 14071; o) A. Castellanos-Gomez, *J. Phy. Chem. Lett.* **2015**, *6*, 4280; p) X. Ling, H. Wang, S. Huang, F. Xia, M. S. Dresselhaus, *Proc. Natl. Acad. Sci. USA* **2015**, *112*, 4523; q) H. Liu, Y. C. Du, Y. X. Deng, P. D. Ye, *Chem. Soc. Rev.* **2015**, *44*, 2732; r) J. Lu, J. Yang, A. Carvalho, H. Liu, Y. Lu, C. H. Sow, *Acc. Chem. Res.* **2016**, *49*, 1806.

[2] a) L. Cartz, S. R. Srinivasa, R. J. Riedner, J. D. Jorgensen, T. G. Worlton, *J. Chem. Phys.* **1979**, *71*, 1718; b) H. Asahina, A. Morita, *J. Phys. C: Solid State Phys.* **1984**, *17*, 1839.

[3] a) G. Nathaniel, W. Darshana, S. Yanmeng, E. Tim, Y. Jiawei, H. Jin, W. Jiang, L. Xue, M. Zhiqiang, W. Kenji, T. Takashi, B. Marc, B. Yafis, K. L. Roger, L. Chun Ning, *2D Mater.* **2015**, *2*, 011001; b) G. Long, D. Maryenko, J. Shen, S. Xu, J. Hou, Z. Wu, W. K. Wong, T. Han, J. Lin, Y. Cai, R. Lortz, N. Wang, *Nano Lett.* **2016**, *16*, 7768.

[4] a) A. Chaves, T. Low, P. Avouris, D. Cakir, F. M. Peeters, *Phys. Rev. B* **2015**, *91*, 155311; b) X. Wang, A. M. Jones, K. L. Seyler, V. Tran,

 

Y. Jia, H. Zhao, H. Wang, L. Yang, X. Xu, F. Xia, *Nat. Nanotechnol.* **2015**, *10*, 517; c) J. Yang, R. Xu, J. Pei, Y. W. Myint, F. Wang, Z. Wang, S. Zhang, Z. Yu, Y. Lu, *Light Sci. Appl.* **2015**, *4*, e312; d) R. Xu, S. Zhang, F. Wang, J. Yang, Z. Wang, J. Pei, Y. W. Myint, B. Xing, Z. Yu, L. Fu, Q. Qin, Y. Lu, *ACS Nano* **2016**, *10*, 2046.

[5] a) D. Li, H. Jussila, L. Karvonen, G. Ye, H. Lipsanen, X. Chen, Z. Sun, *Sci. Rep.* **2015**, *5*, 15899; b) S. Lan, S. Rodrigues, L. Kang, W. Cai, *ACS Photonics* **2016**, *3*, 1176; c) Y. Cai, Q. Ke, G. Zhang, Y. P. Feng, V. B. Shenoy, Y.-W. Zhang, *Adv. Funct. Mater.* **2015**, *25*, 2230; d) J. Kim, J.-U. Lee, J. Lee, H. J. Park, Z. Lee, C. Lee, H. Cheong, *Nanoscale* **2015**, *7*, 18708; e) Y. Gao, *Natl. Sci. Rev.* **2016**, *3*, 158; f) X. Ling, S. Huang, E. H. Hasdeo, L. Liang, W. M. Parkin, Y. Tatsumi, A. R. Nugraha, A. A. Puretzky, P. M. Das, B. G. Sumpter, D. B. Geohegan, J. Kong, R. Saito, M. Drndic, V. Meunier, M. S. Dresselhaus, *Nano Lett.* **2016**, *16*, 2260; g) Z.-Y. Ong, Y. Cai, G. Zhang, Y.-W. Zhang, *J. Phys. Chem. C* **2014**, *118*, 25272; h) L. Q. Su, Y. Zhang, *Appl. Phys. Lett.* **2015**, *107*, 071905; i) J. Tao, W. Shen, S. Wu, L. Liu, Z. Feng, C. Wang, C. Hu, P. Yao, H. Zhang, W. Pang, X. Duan, J. Liu, C. Zhou, D. Zhang, *ACS Nano* **2015**, *9*, 11362; j) F. N. Xia, H. Wang, Y. C. Jia, *Nat. Commun.* **2014**, *5*, 4458.

[6] R. Schuster, J. Trinckauf, C. Habenicht, M. Knupfer, B. Büchner, *Phys. Rev. Lett.* **2015**, *115*, 026404.

[7] a) M. Engel, M. Steiner, P. Avouris, *Nano Lett.* **2014**, *14*, 6414; b) L. Viti, J. Hu, D. Coquillat, W. Knap, A. Tredicucci, A. Politano, M. S. Vitiello, *Adv. Mater.* **2015**, *27*, 5567; c) J. Wu, G. K. W. Koon, D. Xiang, C. Han, C. T. Toh, E. S. Kulkarni, I. Verzhbitskiy, A. Carvalho, A. S. Rodin, S. P. Koenig, G. Eda, W. Chen, A. H. C. Neto, B. Özyilmaz, *ACS Nano* **2015**, *9*, 8070; d) R. Zhang, Y. Zhang, H. Yu, H. Zhang, R. Yang, B. Yang, Z. Liu, J. Wang, *Adv. Opt. Mater.* **2015**, *3*, 1787; e) M. Huang, M. Wang, C. Chen, Z. Ma, X. Li, J. Han, Y. Wu, *Adv. Mater.* **2016**, *28*, 3481; f) N. Mao, S. Zhang, J. Wu, H. Tian, J. Wu, H. Xu, H. Peng, L. Tong, J. Zhang, *Nano Res.* **2017**, https://doi.org/10.1007/s12274-017-1690-4; g) Z. B. Matthew, Y. Zhibin, H. Jianhua, L. Shu Ping, Z. Hui, *2D Mater.* **2017**, *4*, 025063; h) Z. Yang, J. Hao, *Small Methods* **2018**, *2*, 1700296; i) Z. Yang, J. Hao, S. Yuan, S. Lin, H. M. Yau, J. Dai, S. P. Lau, *Adv. Mater.* **2015**, *27*, 3748.

[8] a) Y. Y. Wang, Z. H. Ni, Z. X. Shen, H. M. Wang, Y. H. Wu, *Appl. Phys. Lett.* **2008**, *92*, 043121; b) L. Gao, W. Ren, B. Liu, R. Saito, Z.-S. Wu, S. Li, C. Jiang, F. Li, H.-M. Cheng, *ACS Nano* **2009**, *3*, 933; c) D. Yoon, H. Moon, Y.-W. Son, J. S. Choi, B. H. Park, Y. H. Cha, Y. D. Kim, H. Cheong, *Phys. Rev. B* **2009**, *80*, 125422.

[9] a) A. C. Ferrari, *Solid State Commun.* **2007**, *143*, 47; b) M. S. Dresselhaus, A. Jorio, A. G. Souza, R. Saito, *Philos. Trans. R. Soc., A* **2010**, *368*, 5355; c) N. Ferralis, *J. Mater. Sci.* **2010**, *45*, 5135; d) R. Saito, M. Hofmann, G. Dresselhaus, A. Jorio, M. S. Dresselhaus, *Adv. Phys.* **2011**, *60*, 413; e) A. C. Ferrari, D. M. Basko, *Nat. Nanotechnol.* **2013**, *8*, 235.

[10] a) L. M. Malard, M. A. Pimenta, G. Dresselhaus, M. S. Dresselhaus, *Phys. Rep.* **2009**, *473*, 51; b) M. S. Dresselhaus, A. Jorio, R. Saito, *Annu. Rev. Condens. Matter Phys.*, **2010**, *1*, 89; c) A. A. Balandin, S. Ghosh, W. Bao, I. Calizo, D. Teweldebrhan, F. Miao, C. N. Lau, *Nano Lett.* **2008**, *8*, 902.

[11] N. Mao, J. Wu, B. Han, J. Lin, L. Tong, J. Zhang, *Small* **2016**, *12*, 2627.

[12] a) C. Kaneta, H. Katayama-Yoshida, A. Morita, *Solid State Commun.* **1982**, *44*, 613; b) Y. Fujii, Y. Akahama, S. Endo, S. Narita, Y. Yamada, G. Shirane, *Solid State Commun.* **1982**, *44*, 579; c) S. Sugai, I. Shirotani, *Solid State Commun.* **1985**, *53*, 753; d) C. Kaneta, H. Katayama-Yoshida, A. Morita, *J. Phys. Soc. Jpn.* **1986**, *55*, 1213.

[13] S. Sugai, T. Ueda, K. Murase, *J. Phys. Soc. Jpn.* **1981**, *50*, 3356.

[14] A. Brown, S. Rundqvist, *Acta Crystallogr.* **1965**, *19*, 684.

[15] a) X. Ling, L. Liang, S. Huang, A. A. Puretzky, D. B. Geohegan, B. G. Sumpter, J. Kong, V. Meunier, M. S. Dresselhaus, *Nano Lett.* **2015**, *15*, 4080; b) J. Ribeiro-Soares, R. M. Almeida, L. G. C. Ado, M. S. Dresselhaus, A. Jorio, *Phys. Rev. B* **2015**, *91*, 205421.

[16] a) X. Lu, X. Luo, J. Zhang, S. Y. Quek, Q. Xiong, *Nano Res.* **2016**, *9*, 3559; b) X. Zhang, Q. H. Tan, J. B. Wu, W. Shi, P. H. Tan, *Nanoscale* **2016**, *8*, 6435; c) J. Wu, N. Mao, L. Xie, H. Xu, J. Zhang, *Angew. Chem.* **2015**, *127*, 2366; *Angew. Chem., Int. Ed.* **2015**, *54*, 2366; d) H. B. Ribeiro, M. A. Pimenta, C. J. S. de Matos, *J. Raman S pectrosc.* **2018**, *49*, 76; e) S. Huang, X. Ling, *Small* **2017**, *13*, 1700823.

[17] a) S. Zhang, N. Mao, J. Wu, L. Tong, J. Zhang, Z. Liu, *Small* **2017**, *13*, 1700466; b) J. W. Jiang, B. S. Wang, H. S. Park, *J. Phys.: Condens. Matter* **2016**, *28*, 65401.

[18] R. X. Fei, L. Yang, *Appl. Phys. Lett.* **2014**, *105*, 083120.

[19] S. Appalakondaiah, G. Vaitheeswaran, S. Lebegue, N. E. Christensen, A. Svane, *Phys. Rev. B* **2012**, *86*, 035105.

[20] F. Yanqing, Z. Jian, D. Yongping, M. Feng, D. Chun-Gang, W. Baigeng, W. Xiangang, *J. Phys.: Condens. Matter* **2015**, *27*, 185302.

[21] A. L. Phaneuf-L'Heureux, A. Favron, J. F. Germain, P. Lavoie, P. Desjardins, R. Leonelli, R. Martel, S. Francoeur, *Nano Lett.* **2016**, *16*, 7761.

[22] C.-G. Andres, V. Leonardo, P. Elsa, O. I. Joshua, K. L. Narasimha-Acharya, I. B. Sofya, J. G. Dirk, B. Michele, A. S. Gary, J. V. Alvarez, W. Z. Henny, J. J. Palacios, S. J. v. d. Z. Herre, *2D Mater.* **2014**, *1*, 025001.

[23] Z. Guo, H. Zhang, S. Lu, Z. Wang, S. Tang, J. Shao, Z. Sun, H. Xie, H. Wang, X.-F. Yu, P. K. Chu, *Adv. Funct. Mater.* **2015**, *25*, 6996.

[24] a) Y. Li, S. Yang, J. Li, *J. Phys. Chem. C* **2014**, *118*, 23970; b) S. Liu, N. Huo, S. Gan, Y. Li, Z. Wei, B. Huang, J. Liu, J. Li, H. Chen, *J. Mater. Chem. C* **2015**, *3*, 10974.

[25] A. Favron, E. Gaufres, F. Fossard, A.-L. Phaneuf-Lheureux, N. Y. W. Tang, P. L. Levesque, A. Loiseau, R. Leonelli, S. Francoeur, R. Martel, *Nat. Mater.* **2015**, *14*, 826.

[26] a) R. Loudon, *Adv. Phys.* **1964**, *13*, 423; b) L. Liang, V. Meunier, *Nanoscale* **2014**, *6*, 5394.

[27] X. L. Liu, X. Zhang, M. L. Lin, P. H. Tan, *Chin. Phys. B* **2017**, *26*, 067802.

[28] a) S. Zhang, J. Yang, R. Xu, F. Wang, W. Li, M. Ghufran, Y.-W. Zhang, Z. Yu, G. Zhang, Q. Qin, Y. Lu, *ACS Nano* **2014**, *8*, 9590; b) Z. Luo, J. Maassen, Y. Deng, Y. Du, R. P. Garrelts, M. S. Lundstrom, P. D. Ye, X. Xu, *Nat. Commun.* **2015**, *6*, 8572.

[29] a) W. Lu, X. Ma, Z. Fei, J. Zhou, Z. Zhang, C. Jin, Z. Zhang, *Appl. Phys. Lett.* **2015**, *107*, 021906; b) H. B. Ribeiro, M. A. Pimenta, C. J. de Matos, R. L. Moreira, A. S. Rodin, J. D. Zapata, E. A. de Souza, A. H. Castro Neto, *ACS Nano* **2015**, *9*, 4270.

[30] a) M. Snure, S. Vangala, D. WalkerJr., *Opt. Mater. Express* **2016**, *6*, 1751; b) M. Baibarac, A. Nila, I. Baltog, *RSC Adv.* **2016**, *6*, 58003.

[31] a) S. P. S. Porto, J. A. Giordmaine, T. C. Damen, *Phys. Rev.* **1966**, *147*, 608; b) C. K. Asawa, R. A. Satten, O. M. Stafsudd, *Phys. Rev.* **1968**, *168*, 957; c) D. L. Rousseau, R. E. Miller, G. E. Leroi, *J. Chem. Phys.* **1968**, *48*, 3409; d) A. Chaves, S. P. S. Porto, *Solid State Commun.* **1972**, *10*, 1075.

[32] a) J. Brunen, T. Strach, J. Zegenhagen, M. Cardona, *Phys. C* **1997**, *282–287*, 599; b) T. Strach, J. Brunen, B. Lederle, J. Zegenhagen, M. Cardona, *Phys. Rev. B* **1998**, *57*, 1292.

[33] a) Q. J. Song, H. F. Wang, X. C. Pan, X. L. Xu, Y. L. Wang, Y. P. Li, F. Q. Song, X. G. Wan, Y. Ye, L. Dai, *Sci. Rep.* **2017**, *7*, 1758; b) D. Z. Tan, H. E. Lim, F. J. Wang, N. B. Mohamed, S. Mouri, W. J. Zhang, Y. Miyauchi, M. Ohfuchi, K. Matsuda, *Nano Res.* **2017**, *10*, 546; c) X. L. Xu, Q. J. Song, H. F. Wang, P. Li, K. Zhang, Y. L. Wang, K. Yuan, Z. C. Yang, Y. Ye, L. Dai, *ACS Appl. Mater. Interfaces* **2017**, *9*, 12601; d) Z. H. Zhou, B. C. Wei, C. Y. He, Y. M. Min, C. H. Chen, L. Z. Liu, X. L. Wu, *Appl. Surf. Sci.* **2017**, *404*, 276; e) Y. Kim, Y. I. Jhon, J. Park, J. H. Kim, S. Lee, Y. M. Jhon,

*Nanoscale* **2016**, *8*, 2309; f) C. Yan, S. Natalya, L. Liangbo, Y. Hui, Z. Tingting, M. Vincent, P. Minghu, *2D Mater.* **2017**, *4*, 035024; g) Q. Song, X. Pan, H. Wang, K. Zhang, Q. Tan, P. Li, Y. Wan, Y. Wang, X. Xu, M. Lin, X. Wan, F. Song, L. Dai, *Sci. Rep.* **2016**, *6*, 29254; h) S. Huang, Y. Tatsumi, X. Ling, H. Guo, Z. Wang, G. Watson, A. A. Puretzky, D. B. Geohegan, J. Kong, J. Li, T. Yang, R. Saito, M. S. Dresselhaus, *ACS Nano* **2016**, *10*, 8964; i) J. Xia, X.-Z. Li, X. Huang, N. Mao, D.-D. Zhu, L. Wang, H. Xu, X.-M. Meng, *Nanoscale* **2016**, *8*, 2063.

[34] P. Alonso-Gutiérrez, M. L. Sanjuán, M. C. Morón, *Phys. Rev. B* **2005**, *71*, 085205.

[35] A. Jorio, R. Saito, G. Dresselhaus, M. S. Dresselhaus, in *Raman Spectroscopy in Graphene Related Systems*, Wiley-VCH, Weinheim, Germany **2011**.

[36] a) J.-W. Jiang, B.-S. Wang, H. S. Park, *J. Phys.: Condens. Matter* **2016**, *28*, 165401; b) J. Ji, S. Dong, A. Zhang, Q. Zhang, *Phys. E* **2016**, *80*, 130.

[37] a) S. Dong, A. Zhang, K. Liu, J. Ji, Y. G. Ye, X. G. Luo, X. H. Chen, X. Ma, Y. Jie, C. Chen, X. Wang, Q. Zhang, *Phys. Rev. Lett.* **2016**, *116*, 087401; b) J. Wu, H. Xu, W. Mu, L. Xie, X. Ling, J. Kong, M. S. Dresselhaus, J. Zhang, *J. Phys. Chem. C* **2014**, *118*, 3636.

[38] X. Luo, X. Lu, G. K. W. Koon, A. H. Castro Neto, B. Özyilmaz, Q. Xiong, S. Y. Quek, *Nano Lett.* **2015**, *15*, 3931.

[39] a) P. H. Tan, W. P. Han, W. J. Zhao, Z. H. Wu, K. Chang, H. Wang, Y. F. Wang, N. Bonini, N. Marzari, N. Pugno, G. Savini, A. Lombardo, A. C. Ferrari, *Nat. Mater.* **2012**, *11*, 294; b) J. X. Wu, H. Xu, J. Zhang, *Acta Chim. Sin.* **2014**, *72*, 301.

[40] a) V. Sorkin, Y. W. Zhang, *Nanotechnology* **2015**, *26*, 235707; b) V. Tran, L. Yang, *Phys. Rev. B* **2014**, *89*, 245407; c) H. Guo, N. Lu, J. Dai, X. Wu, X. C. Zeng, *J. Phys. Chem. C* **2014**, *118*, 14051; d) Y. Lee, J. Y. Yoon, D. Scullion, J. Jang, E. J. G. Santos, H. Y. Jeong, K. Kim, *J. Phys. D: Appl. Phys.* **2017**, *50*, 084003; e) Y. Nakanishi, A. Ishi, C. Ohata, D. Soriano, R. Iwaki, K. Nomura, M. Hasegawa, T. Nakamura, S. Katsumoto, S. Roche, J. Haruyama, *Nano Res.* **2017**, *10*, 718; f) Z. W. Bao, H. W. Wu, Y. Zhou, *Appl. Phys. Lett.* **2016**, *109*, 241902; g) L. Liang, J. Wang, W. Lin, B. G. Sumpter, V. Meunier, M. Pan, *Nano Lett.* **2014**, *14*, 6400.

[41] Y. Taka-aki, Y. Keisuke, H. Yuhei, H. Tomohiro, O. Fumio, H. Masahiko, *2D Mater.* **2015**, *2*, 035004.

[42] a) D. J. Late, *ACS Appl. Mater. Interfaces* **2015**, *7*, 5857; b) A. Łapińska, A. Taube, J. Judek, M. Zdrojek, *J. Phys. Chem. C* **2016**, *120*, 5265; c) A. S. Pawbake, M. B. Erande, S. R. Jadkar, D. J. Late, *RSC Adv.* **2016**, *6*, 76551; d) L. Su, Y. Zhang, *Appl. Phys. Lett.* **2015**, *107*, 071905; e) Z.-P. Ling, K.-W. Ang, *APL Mater.* **2015**, *3*, 126104.

[43] N. Bonini, M. Lazzeri, N. Marzari, F. Mauri, *Phys. Rev. Lett.* **2007**, *99*.

[44] I. Calizo, A. A. Balandin, W. Bao, F. Miao, C. N. Lau, *Nano Lett.* **2007**, *7*, 2645.

[45] S. Sahoo, A. P. S. Gaur, M. Ahmadi, M. J. F. Guinel, R. S. Katiyar, *J. Phys. Chem. C* **2013**, *117*, 9042.

[46] P. Venezuela, M. Lazzeri, F. Mauri, *Phys. Rev. B* **2011**, *84*, 035433.

[47] a) Z. J. Xiang, G. J. Ye, C. Shang, B. Lei, N. Z. Wang, K. S. Yang, D. Y. Liu, F. B. Meng, X. G. Luo, L. J. Zou, Z. Sun, Y. Zhang, X. H. Chen, *Phys. Rev. Lett.* **2015**, *115*, 186403; b) P.-L. Gong, D.-Y. Liu, K.-S. Yang, Z.-J. Xiang, X.-H. Chen, Z. Zeng, S.-Q. Shen, L.-J. Zou, *Phys. Rev. B* **2016**, *93*, 195434.

[48] a) S. N. Gupta, A. Singh, K. Pal, B. Chakraborti, D. V. S. Muthu, U. V. Waghmare, A. K. Sood, *Phys. Rev. B* **2017**, *96*, 094104; b) S. Taizo, K. Kensuke, A. Yuichi, N. Satoshi, T. Takashi, *Jpn. J. Appl. Phys.* **2017**, *56*, 05FB06; c) Y. Akahama, M. Kobayashi, H. Kawamura, *Solid State Commun.* **1997**, *104*, 311.

[49] a) J. Feng, X. F. Qian, C. W. Huang, J. Li, *Nat. Photonics* **2012**, *6*, 865; b) C. Lee, X. Wei, J. W. Kysar, J. Hone, *Science* **2008**, *321*, 385; c) J. Quereda, P. San-Jose, V. Parente, L. Vaquero-Garzon, A. J. Molina-Mendoza, N. Agrait, G. Rubio-Bollinger, F. Guinea, R. Roldan, A. Castellanos-Gomez, *Nano Lett.* **2016**, *16*, 2931.

[50] a) X. H. Peng, Q. Wei, A. Copple, *Phys. Rev. B* **2014**, *90*, 085402; b) T. Zhang, J.-H. Lin, Y.-M. Yu, X.-R. Chen, W.-M. Liu, *Sci. Rep.* **2015**, *5*, 13927; c) C.-X. Wang, C. Zhang, J.-W. Jiang, H. S. Park, T. Rabczuk, *Nanoscale* **2016**, *8*, 901.

[51] a) A. S. Rodin, A. Carvalho, A. H. Castro Neto, *Phys. Rev. Lett.* **2014**, *112*, 176801; b) A. Jain, A. J. McGaughey, *Sci. Rep.* **2015**, *5*, 8501; c) P. San-Jose, V. Parente, F. Guinea, R. Roldán, E. Prada, *Phys. Rev. X* **2016**, *6*, 031046.

[52] a) Y. L. Wang, C. X. Cong, R. X. Fei, W. H. Yang, Y. Chen, B. C. Cao, L. Yang, T. Yu, *Nano Res.* **2015**, *8*, 3944; b) Y. Li, Z. Hu, S. Lin, S. K. Lai, W. Ji, S. P. Lau, *Adv. Funct. Mater.* **2017**, *27*, 1600986.

[53] a) M. Huang, H. Yan, C. Chen, D. Song, T. F. Heinz, J. Hone, *Proc. Natl. Acad. Sci. USA* **2009**, *106*, 7304; b) T. M. G. Mohiuddin, A. Lombardo, R. R. Nair, A. Bonetti, G. Savini, R. Jalil, N. Bonini, D. M. Basko, C. Galiotis, N. Marzari, K. S. Novoselov, A. K. Geim, A. C. Ferrari, *Phys. Rev. B* **2009**, *79*, 205433; c) C. Rice, R. J. Young, R. Zan, U. Bangert, D. Wolverson, T. Georgiou, R. Jalil, K. S. Novoselov, *Phys. Rev. B* **2013**, *87*, 081307.

[54] L. Kou, Y. Ma, S. C. Smith, C. Chen, *J. Phy. Chem. Lett.* **2015**, *6*, 1509.

[55] Y. Wang, C. Cong, R. Fei, W. Yang, Y. Chen, B. Cao, L. Yang, T. Yu, *Nano Res.* **2015**, *8*, 3944.